creative commons
COMMONS DEED

저작자표시 2.0 대한민국

이용자는 아래의 조건을 따르는 경우에 한하여 자유롭게

- 이 저작물을 복제, 배포, 전송, 전시, 공연 및 방송할 수 있습니다.
- 이차적 저작물을 작성할 수 있습니다.
- 이 저작물을 영리 목적으로 이용할 수 있습니다.

다음과 같은 조건을 따라야 합니다:

저작자표시. 귀하는 원저작자를 표시하여야 합니다.

- 귀하는, 이 저작물의 재이용이나 배포의 경우, 이 저작물에 적용된 이용허락조건을 명확하게 나타내어야 합니다.
- 저작권자로부터 별도의 허가를 받으면 이러한 조건들은 적용되지 않습니다.

저작권법에 따른 이용자의 권리는 위의 내용에 의하여 영향을 받지 않습니다.

이것은 이용허락규약(Legal Code)을 이해하기 쉽게 요약한 것입니다.

Disclaimer

dCollection

공학박사 학위논문

Advanced Metrology for High-k Films and Bulge-free Process for Grayscale Lithography via Versatile AFM

다기능 AFM을 통한 고유전율 박막의 고급 계측 및 3차원 리소그래피를 위한 벌지 제거 연구

2019년 2월

서울대학교 융합과학기술대학원

나노융합학과 나노융합전공

문 승 현

Advanced Metrology for High-k Films and Bulge-free Process for Grayscale Lithography via Versatile AFM

지도교수 김 연 상

이 논문을 공학박사학위 논문으로 제출함.

2019년 2월

서울대학교 융합과학기술대학원
나노융합학과 나노융합전공

문 승 현

문승현의 박사학위 논문을 인증함
2019 년 1 월

위 원 장 박 원 철 인

부위원장 김 연 상 인

위 원 이 강 원 인

위 원 신 채 호 인

위 원 최 지 훈 인

Advanced Metrology for High-k Films and Bulge-free Process for Grayscale Lithography via Versatile AFM

Seunghyun Moon

Supervised by

Professor Youn Sang Kim

A Dissertation

Submitted to the Faculty of Seoul National University

In Partial Fulfillment of the Requirements

For the Degree of Doctor of Philosophy

February 2019

Department of Nano Science and Technology

Graduate School of Convergence Science and Technology

Seoul National University

Abstract

Advanced Metrology for High-k Films and Bulge-free Process for Grayscale Lithography via Versatile AFM

Seunghyun Moon

Department of Nano Science and Technology

Graduate School of Convergence Science & Technology

Seoul National University

Scanning probe microscopy (SPM) is widely used to analyze the surface structures and properties of semiconductor and bio-molecular films. The merits of the SPM method are that it does not require any process for sample preparation and minimizes damages of the probing sample. Moreover, the growth of industries related to semiconductor and nano-bio devices has led to the development of nanotechnology. Many researchers now become aware of the importance of local

variations, such as the local doping profiles of semiconductors, the work function of two-dimensional materials, the surface profiles of bio-molecular films, the diodic behavior of nanofluidic devices, the surface roughness of semiconductor thin films, and the distribution of local surface charge. Thus, the researchers are seeking appropriate SPM equipment to analyze the local variations.

In recent years, atomic force microscopes have emerged that can perform various functions. Especially, low-noise atomic force microscopy can be used to measure linewidths of nanoscale next-generation semiconductors or inspection for ultra-thin films. Therefore, Korea Research Institute of Standards and Science has developed a low noise atomic force microscope considering the industrial application. As well as, it has been developed to perform sophisticated nano/micro patterns by adding the function of nano-indentation.

The low-noise atomic force microscope avoids the installation of an internal stage due to the nature of the development background. Although it contributes significantly to the signal integrity of the low-noise atomic force microscope, it serves as a weakness to limit the scan area of the test sample. Therefore, it is essential to have an independent external stage to compensate the weakness. In this paper, we have developed the middle range moving stage for the measurements of the standard reference samples. The maximum travel length of the external 4-axis

stage is 10 mm. For image scanning of a specific area of interest, the sample is positioned with micron accuracy through an external stage and then finely positioned using a PI XY piezo scanner. We confirmed that the position error of the developed stage can be ignored by the reproducibility experiment. Subsequently, the sidewall of the improved vertical parallel structure (IVPS) was measured. The repeatability and reproducibility (R&R) of the CD measurement was estimated using the CDR30-EBD tip. Finally, we found that the tip wear was minimized by measuring the TGX1 sample with the undercut structure. Thus, the development of independent external stages can be useful for many tasks that require large scanning areas.

In the industrial semiconductor fabrication, the inspection of thin films is performed through optical equipment to check the uniformity of wafers. In the next-generation semiconductor industry, high-capacity and low-power devices with complex lithography patterns and ultra-thin insulating films are emerging. Therefore, in order to improve the yield of semiconductor devices, it is necessary to inspect not only the thickness of these thin films but also local variations. Indeed, the surface roughness of the semiconductor process may affect the formation of the ultrathin film, and even if the process of the ultra-thin films is optimized by the atomic layer deposition (ALD), the performance of the device may be degraded due to the

roughened surface. Therefore, atomic force microscopy is the most suitable method for quantifying the properties of thin films and for analyzing the local surface structures.

In this thesis, critical roughness (CR) was defined for the first time in a nanoscale by devising a roughness scaling process as a method for managing hafnium oxide film, which is a high-k insulating film of a MOS transistor. The surface roughness of the substrate was processed by a wet etching method, and an ALD process was used to obtain a hafnium oxide film. This is a study on the influence of the roughness of the lower layer on the roughness of the upper layer, and this definition makes it possible to present the criteria of the standard production in the in-line oxide film process. Moreover, we confirmed that the CR value defined in this study was effective by realizing the MIM diode structures with different roughness.

Furthermore, new research methods were introduced through the indentation lithography. The first study suggests that nano- and micro-patterns can be formed on biofilms that is impracticable by electron beam lithography. The indentation method can be a means to compensate the weaknesses of electron beam lithography. The second study is to selectively remove the bulges generated during the indentation process. For many years, it was a quite important issue because the formation of the

bulge was a major factor impeding the development of indentation technology.

All in all, in this thesis, various research themes realized by the multi-functional AFM are presented. The new definition of the roughness contributed to the in-line process control. The patterned biofilm could be used as a standard sample of the TOF-SIMS imaging. The selective removal of the bulges suggested a new method for three-dimensional nanolithography. Therefore, this research is expected to be a cost effective technology in the industry and to be used in various research fields.

Kew words:

AFM, Indentation lithography, Critical roughness, Atomic layer deposition, Grayscale lithography, Bulge-free indentation

Student number: 2010-31262

Contents

List of Figures

List of Tables

Chapter 1 Introduction

1.1 Multifunctional atomic force microscopy

Atomic force microscope (AFM) is a third-generation microscope widely used in research fields and industry, along with optical microscopes and electron microscopes. As a sub-concept of scanning probe microscope (SPM), it is scanned through the probe to obtain images. AFM is now an indispensable metrology tool that is capable of reliably and accurately observing surface structures in a nondestructive way [1-6]. It directly assesses the surface morphology and roughness with a sub-nanometer spatial resolution. For example, the metal etch-back (MEB) depth profiles of dynamic random-access memory (DRAM), for which no signal can be detected by spectroscopic ellipsometry (SE), can be examined by using inline automated AFM (AAFM). In addition, roughness examinations of the ultrathin films without any interference from the lower membrane can be implemented [5, 7].

In spite of the fact that it is a relatively slow imaging technology, AFM has been adopted in many fields. As well as, it can be supplied at a low cost. Thus, expanding the ability to utilize such AFM equipment has become a demand for current researchers. For examples, the history that AFM technology has used to stimulate soft cell surfaces and begin to utilize it as a bio-imaging technology dates back a

long time [8, 9]. A frequency-modulation method in electric force microscopy or kelvin probe force microscopy enabled us to monitor the local charge distributions [10]. Surprisingly, the function of the AFM is now being extended to the lithographic technique [11-14]. It is worthy that indentation lithography is a cost-effective lithography technique that is less susceptible to materials or substrates. However, the main factor impeding the development of indentation lithography is the occurrence of bulge. Particularly, the bulge formed at the moment of pressing into the polymer is difficult to remove. Moreover, three dimensional (3D) patterning technique is a critical issue to be solved through the AFM technique because the pressing force can be controlled by the equipment.

1.2 Background on development of external stage for low noise AFM

The signals taken by the automated AFM in the industrial field contain various noise. In this circumstance, it is more efficient to remove the specific frequency using software filtering technology than to find and eliminate the cause of the noise. Based on the background knowledge, we have designed minimized mechanical components for low noise atomic force microscope (LN-AFM) design. That is, to supply accurate surface information and to improve the signal-to-noise ratio (SNR),

mechanical components, such as an automation stage, should be excluded.

The LN-AFM is supposed to measure the surface of thin films or variations of nanostructures [15, 16]. Likewise, AFM manufacturers and a lot of researchers suggested novel measurement methods for various samples to supply more sophisticated surface profiles and more improved signal-to-noise ratios (SNRs) by using robust hardware configurations or by eliminating noise via software filters [10, 17-19]. However, low noise technology and sample mobility still conflict each other.

Even if the noise problem is solved, AFM continues to have reliability problems due to tip wear, which can distort the force strength between the sample and the probe. Even with the use of durable diamond-like carbon (DLC) coated tips or high-density carbon (HDC) probes to avoid abrasion, the tip-wearing problem is inevitable. Particularly in special circumstances such as sidewall measurements or critical dimension (CD) metrology, the target sample has to be traveled at least in a few millimeters. In addition, minimum trials and precise measurements should be conducted at the location because an increased number of measurements due to position errors can lead to probe abrasion [20-23].

Accordingly, an independent external stage that enables the measurements of critical dimensions (CDs) by the LN-AFM was suggested in this thesis. It was confirmed that the position errors caused by the external stage and the tip stage were

negligible through the reproducibility study and the AFM indentation method. Furthermore, by securing the capability of positioning, unlimited applications such as CD measurements, surface inspections, and large area processing of indentation lithography will be expected through the external stage.

1.3 Industrial applications for low noise atomic force microscopy

1.3.1 Critical dimension

The demand for mobile devices, the internet of things (IoT), and artificial intelligence (AI) has increased dramatically, and the semiconductor industry is also making efforts to expand supply. Especially, as new insulating materials and multilayer techniques are introduced, a thickness metrology for ultrathin films is becoming significant. Thus, new industrial criteria are required to enhance production yield and stable process control through reliable inline metrology together with an increasing production scale. Thickness metrology now requires quantitative methods for surface topology and interface effects between each multilayer film as well as thickness measurement. For that purpose, roughness metrology through nanometer- or angstrom-level process control will reinforce the

thickness metrology because the roughness of the ultrathin films directly impacts the local thickness of the films, which can affect the performance and lifetime of the devices.

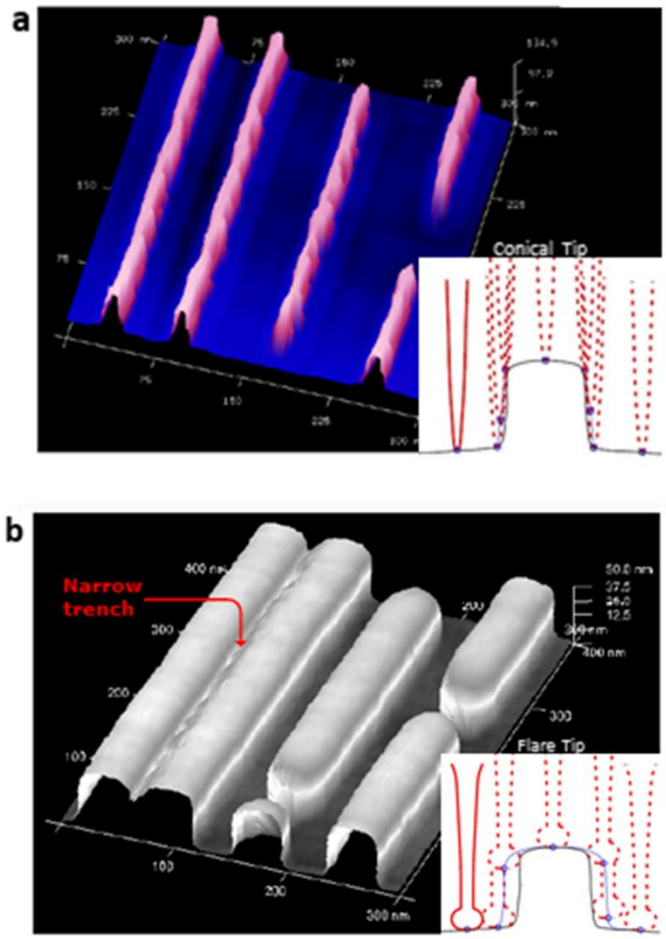

Figure 1.1 (a) Logic 2X SRAM Finfet structure images. DT tip was used. (tip diameter ~ 10 nm) (inset: when using conical tip.) (b) CD AFM image of Logic 2X SRAM FinFet structure using Insight Bruker inline CD-AFM. CDR20-EBD tip was used (tip head: 20 nm). Scan area is field of view of 300 nm × 400 nm with CD mode. (inset: when using flare tip)

1.3.2 Emergence of ultrathin films

In relation to current industrial semiconductor metrology, the management of the thickness of ultrathin films has been conducted in a strict manner. Electron microscope studies, such as vertical scanning electron microscopy (VSEM) and transmission electron microscopy (TEM), are crucial to accurately measuring the thickness of ultrathin films and calibrating optical thickness measurement tools. These instruments are used to measure the films directly, but practical uses are difficult for inline metrology due to the potential damage to the device during the destructive sampling process [24-27].

Ellipsometry is a common approach to managing the thickness of the transparent and translucent films used in the semiconductor manufacturing process because this method is fast and nondestructive [28-30]. The film thickness can be calculated from measuring optical constants, such as the reflection coefficients and phase changes, by detecting the polarized light reflected from the thin film. Although spectral ellipsometry is a powerful tool when managing film thicknesses at the angstrom (Å) level using a proper micrometer spot size on the illuminated areas, it does not provide sub-nanoscale local surface information due to the limited lateral resolution associated with this method [31, 32].

In recent years, a great deal of attraction has been paid to improve the

performance of the AFM because of the surge of interest in the ultrathin films. Many efforts have been made to replace the gate SiO_2 (K = 3.9) layer with a high dielectric constant (K) to reduce the tunneling current and ensure low power consumption for a complementary metal-oxide semiconductor (CMOS) [33-35]. Among high dielectric constant materials, hafnium oxide (HfO_2) films are being used in the semiconductor industry due to their relatively high K values (K = 25) and large band gaps [36]. However, the reliability of HfO_2 thin films comes into question on multiple layers due to the poor interfacial quality and inferior thermal stability between the Hf atoms [37-40]. Therefore, providing the criteria pertaining to sub-nanoscale surface roughness is becoming an important task.

1.4 Applications of indentation lithography using low noise atomic force microscopy

1.4.1 Demand for biological applications

From the example of the brain slice image of a rat, we can find easily the different contrast images of the same bio molecular. Showing different image shapes depending on the primary beam source is acting as a stumbling block to bio-applications of time-of-flight secondary ion mass spectrometry (TOF-SIMS) [41].

Therefore, it is necessary to carry out a calibration process with already known bio standard samples.

Many researchers have been achieved for the biologicals applications of TOF-SIMS equipment [42-45]. Secondary ion mass spectrometry (SIMS) has been a powerful tool for chemical imaging and depth analysis. Especially, gas cluster ion sources (GCIB) in SIMS analysis have widely used not only as a primarily source for surface analysis but also as an erosion source which has a low damage cross section and a fast erosion rate for molecular depth profiling experiments. However, in order to understand an erosion mechanism for 3D depth profile in SIMS analysis, it is necessary to calibrate with a well-defined 3D organic micro-patterns. However, only two-dimensional (2D) patterns or non-patterned three-dimensional layers are being studied [46, 47]. This is because it is a quite challenging work to make 3D organic patterns for image analysis by traditional methods. Therefore, indentation lithography is the excellent candidate for making patterns on bio-films

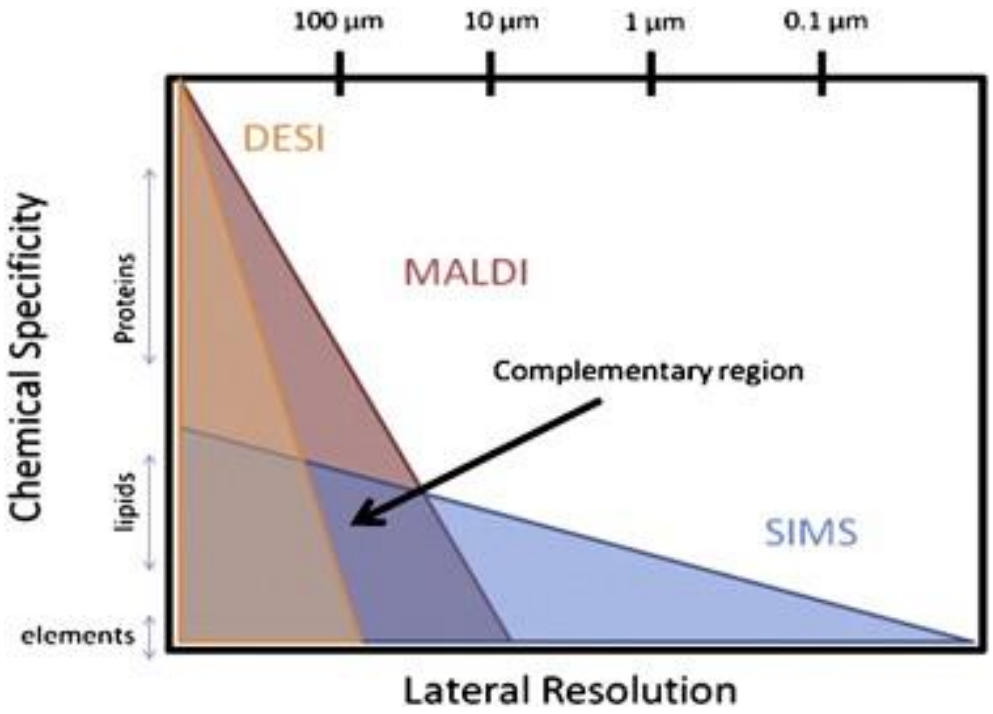

Figure 1.2 The diagram describes overlaps and unique area of MALDI, DESI and SIMS. Lipids are detectable in all three methodologies. (Reprinted with permission from reference [44] of chapter 1.)

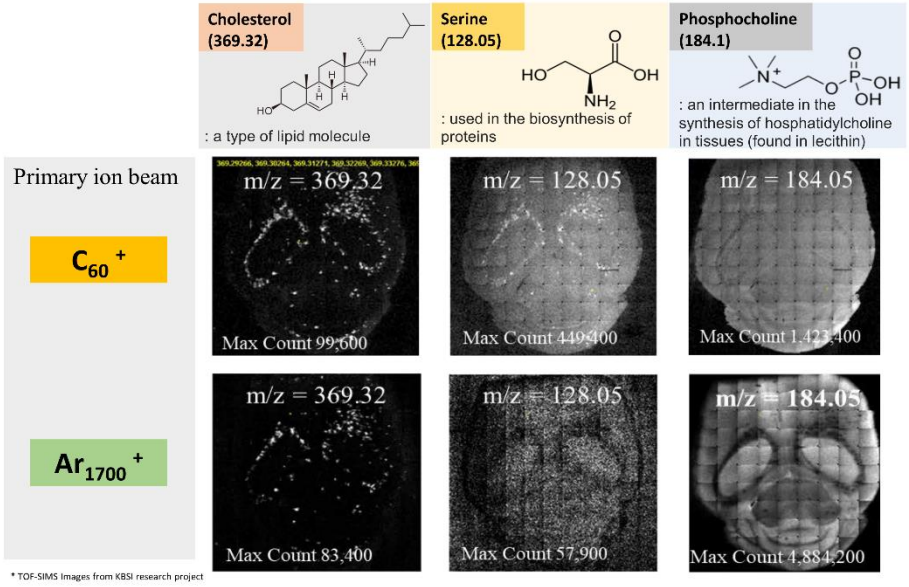

Figure 1.3 Example of TOF-SIMS imaging. Brain slice image of a rat.

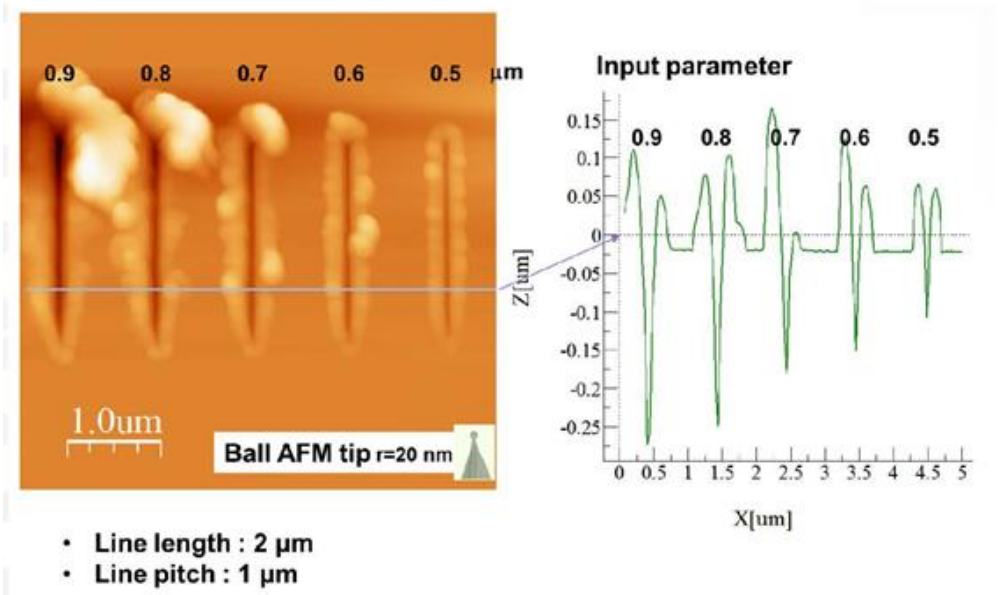

Figure 1.4 Indentation line patterns formed on the trehalose biofilm using a ball tip. Different depth profiles are formed depending on the strength of the pressing force. The numbers represent the relative strength of the pressing force.

1.4.2 Various lithography techniques

Lithography technology is key technique for research fields and industry. The technique is directly connected with the production of nano-bio sensors [48, 49], nano/micro fluidic devices [50], optoelectronic devices [51], and plasmonic templates [52] and capable of producing various nano/micro structures on a desired substrate.

Conventional nanofabrication technologies such as electron beam (E-beam) lithography, focused ion beam (FIB) and extreme ultraviolet (EUV) lithography have dominated nanostructure fabrication to provide unprecedented resolution. However, these techniques have the disadvantage of requiring capital equipment, and there is still a need for accessible nano-pattern lithography in many research areas. For this reason, techniques such as nanoimprint lithography, colloid lithography, and dip-pen nanolithography have been developed to overcome the weakness of the conventional techniques [53].

1.4.3 Strengths and limitations of AFM indentation lithography

AFM indentation lithography is a promising technique because it has several

advantages. For example, it can be written directly on a substrate without a mask. The patterning can be conducted regardless of organic/inorganic materials, or biomaterials. AFM is already widely available equipment. It is not necessary to consider the pretreatment process of the sample or the charging effect. It is another merit that inspection can be performed immediately after the patterning.

However, in terms of technical completeness, the following problems should be solved. i) The first drawback is wear of the probe induced by the indentation process. An attempt to use diamond probes is the effort to address this problem. ii) Second problem of indentation lithography is low throughput. It takes minutes to acquire an image or make dent patterns on the sample surface because the scan speed is limited by the piezotube. It is inadequate for the industrial demands to make wafer-scale patterns. However, in near future, the problem will be solved with a high-speed and multi probes AFM. iii) The final difficulty is the unintended formations (or protrusions) which are piled around the indentation patterns. Unlike the conventional lithography method, this is the most serious and inevitable problem for the AFM indentation lithography. The bulge is formed in an asymmetrical shape and formed in various sizes depending on the tip shape, the hardness of the polymer resist, and the tip loading force. These protrusions must be addressed to broaden the application range of the AFM indentation process. In addition, this bulging problem

hinders the fabrication of multi-layered patterns with micro and nanometer scales.

1.5. The aims of this study

The goals of this thesis are to maximize the use of LN-AFM equipment. So both industrial and academic applications will be introduced. The industrial applications will contribute to the next generation semiconductor metrology by measuring CD and defining critical roughness. Therefore, a stage capable of extending the scanning area of the sample is essential.

This paper also reports the patterning method on biomaterials. This patterned bio-sample will be used as a reference sample for the TOF-SIMS imaging. Furthermore, the selective bulge removal in a very simple process will open a new era in 3D nanolithography.

1.6. Reference

[1] Y. Sugimoto, P. Pou, M. Abe, P. Jelinek, R. Pérez, S. Morita, Ó. Custance, Chemical identification of individual surface atoms by atomic force microscopy, *Nature*, 446, **2007**, 64.

[2] H.-J. Butt, B. Cappella, M. Kappl, Force measurements with the atomic force microscope: Technique, interpretation and applications, *Surf. Sci. Rep.*, 59, **2005**, 1-152.

[3] W. Melitz, J. Shen, A.C. Kummel, S. Lee, Kelvin probe force microscopy and its application, *Surf. Sci. Rep.*, 66, **2011**, 1-27.

[4] J.S. Lee, J. Song, S.O. Kim, S. Kim, W. Lee, J.A. Jackman, D. Kim, N.-J. Cho, J. Lee, Multifunctional hydrogel nano-probes for atomic force microscopy, *Nat. Commun.*, 7, **2016**, 11566.

[5] C. Shin, K. Kim, J. Kim, W. Ko, Y. Yang, S. Lee, C.S. Jun, Y.S. Kim, Fast, exact, and non-destructive diagnoses of contact failures in nano-scale semiconductor device using conductive AFM, *Sci. Rep.*, 3, **2013**, 2088.

[6] M. Kocun, A. Labuda, W. Meinhold, I. Revenko, R. Proksch, Fast, High Resolution, and Wide Modulus Range Nanomechanical Mapping with Bimodal Tapping Mode, *ACS Nano*, 11, **2017**, 10097-10105.

[7] S. Narasimha, P. Chang, C. Ortolland, D. Fried, E. Engbrecht, K. Nummy, P. Parries, T. Ando, M. Aquilino, N. Arnold, 22nm High-performance SOI technology featuring dual-embedded stressors, Epi-Plate High-K deep-trench embedded DRAM and self-aligned Via 15LM BEOL, in: Electron Devices Meeting (IEDM), 2012 IEEE International, *IEEE*, **2012**, pp. 3.3. 1-3.3. 4.

[8] H. Wu, T. Kuhn, V. Moy, Mechanical properties of L929 cells measured by atomic force microscopy: effects of anticytoskeletal drugs and membrane crosslinking, *Scanning: The Journal of Scanning Microscopies*, 20, **1998**, 389-397.

[9] Q. Li, G.Y. Lee, C.N. Ong, C.T. Lim, AFM indentation study of breast cancer cells, *Biochemical and biophysical research communications*, 374, **2008**, 609-613.

[10] S. Moon, M. Kang, J.-H. Kim, K.-R. Park, C. Shin, Creation of Optimal Frequency for Electrostatic Force Microscopy Using Direct Digital Synthesizer, *Applied Sciences*, 7, **2017**, 704.

[11] C.F. Quate, Scanning probes as a lithography tool for nanostructures, *Surface Science*, 386, **1997**, 259-264.

[12] S. Hu, A. Hamidi, S. Altmeyer, T. Köster, B. Spangenberg, H. Kurz, Fabrication of silicon and metal nanowires and dots using mechanical atomic

force lithography, *Journal of Vacuum Science & Technology B: Microelectronics and Nanometer Structures Processing, Measurement, and Phenomena*, 16, **1998**, 2822-2824.

[13] J. Gong, D.J. Lipomi, J. Deng, Z. Nie, X. Chen, N.X. Randall, R. Nair, G.M. Whitesides, Micro-and nanopatterning of inorganic and polymeric substrates by indentation lithography, *Nano letters*, 10, **2010**, 2702-2708.

[14] L.L. Cheong, P. Paul, F. Holzner, M. Despont, D.J. Coady, J.L. Hedrick, R. Allen, A.W. Knoll, U. Duerig, Thermal probe maskless lithography for 27.5 nm half-pitch Si technology, *Nano letters*, 13, **2013**, 4485-4491.

[15] T. Fukuma, M. Kimura, K. Kobayashi, K. Matsushige, H. Yamada, Development of low noise cantilever deflection sensor for multienvironment frequency-modulation atomic force microscopy, *Review of Scientific Instruments*, 76, **2005**, 053704.

[16] T.R. Albrecht, C. Quate, Atomic resolution imaging of a nonconductor by atomic force microscopy, *Journal of Applied Physics*, 62, **1987**, 2599-2602.

[17] S.-J. Cho, B.-W. Ahn, J. Kim, J.-M. Lee, Y. Hua, Y.K. Yoo, S.-i. Park, Three-dimensional imaging of undercut and sidewall structures by atomic force microscopy, *Review of Scientific Instruments*, 82, **2011**, 023707.

[18] C. Shin, I. Jeon, Z.G. Khim, J. Hong, H. Nam, Study of sensitivity and noise in the piezoelectric self-sensing and self-actuating cantilever with an integrated Wheatstone bridge circuit, *Review of Scientific Instruments*, 81, **2010**, 035109.

[19] T. Bao, D. Fong, S. Hand, Automated AFM as an Industrial Process Metrology Tool for Nanoelectronic Manufacturing, in: Applied Scanning Probe Methods X, *Springer*, **2008**, pp. 359-412.

[20] D. Hussain, K. Ahmad, J. Song, H. Xie, Advances in the atomic force microscopy for critical dimension metrology, *Measurement Science and Technology*, 28, **2016**, 012001.

[21] N.G. Orji, H. Itoh, C. Wang, R.G. Dixson, P.S. Walecki, S.W. Schmidt, B. Irmer, Tip characterization method using multi-feature characterizer for CD-AFM, *Ultramicroscopy*, 162, **2016**, 25-34.

[22] H. Xie, D. Hussain, F. Yang, L. Sun, Atomic force microscope caliper for critical dimension measurements of micro and nanostructures through sidewall scanning, *Ultramicroscopy*, 158, **2015**, 8-16.

[23] F. Tian, X. Qian, J.S. Villarrubia, Blind estimation of general tip shape in AFM imaging, *Ultramicroscopy*, 109, **2008**, 44-53.

[24] S.H. Rha, J. Jung, Y.S. Jung, Y.J. Chung, U.K. Kim, E.S. Hwang, B.K.

Park, T.J. Park, J.-H. Choi, C.S. Hwang, Vertically integrated submicron amorphous-In2Ga2ZnO7 thin film transistor using a low temperature process, *Appl. Phys. Lett.*, 100, **2012**, 203510.

[25] F.A. Stevie, C.B. Vartuli, L.A. Giannuzzi, T.L. Shofner, S.R. Brown, B. Rossie, F. Hillion, R.H. Mills, M. Antonell, R.B. Irwin, B.M. Purcell, Application of focused ion beam lift-out specimen preparation to TEM, SEM, STEM, AES and SIMS analysis, *Surf. Interface Anal.*, 31, **2001**, 345-351.

[26] M. Baram, W.D. Kaplan, Quantitative HRTEM analysis of FIB prepared specimens, *J. Microsc.*, 232, **2008**, 395-405.

[27] W. Wang, D. Lei, Y. Dong, X. Gong, E.S. Tok, Y.-C. Yeo, Digital Etch Technique for Forming Ultra-Scaled Germanium-Tin (Ge 1−x Sn x) Fin Structure, *Sci. Rep.*, 7, **2017**, 1835.

[28] M. Losurdo, K. Hingerl, Ellipsometry at the Nanoscale, *Springer Science & Business Media*, **2013**.

[29] C.S. Cook, T. Daly, R. Liu, M. Canonico, Q. Xie, R. Gregory, S. Zollner, Spectroscopic ellipsometry for in-line monitoring of silicon nitrides, *Thin Solid Films*, 455, **2004**, 794-797.

[30] A.C. Diebold, F.J. Nelson, V.K. Kamineni, Spectroscopic ellipsometry of nanoscale materials for semiconductor device applications, in: Ellipsometry

at the Nanoscale, *Springer*, **2013**, pp. 557-581.

[31] P. Karageorgiev, H. Orendi, B. Stiller, L. Brehmer, Scanning near-field ellipsometric microscope-imaging ellipsometry with a lateral resolution in nanometer range, *Applied Physics Letters*, 79, **2001**, 1730-1732.

[32] C. Edwards, A. Arbabi, G. Popescu, L.L. Goddard, Optically monitoring and controlling nanoscale topography during semiconductor etching, *Light: Science & Applications*, 1, **2012**, e30.

[33] A. Liu, R. Jones, L. Liao, D. Samara-Rubio, D. Rubin, O. Cohen, R. Nicolaescu, M. Paniccia, A high-speed silicon optical modulator based on a metal–oxide–semiconductor capacitor, *Nature*, 427, **2004**, 615.

[34] V.A. Gritsenko, T.V. Perevalov, D.R. Islamov, Electronic properties of hafnium oxide: A contribution from defects and traps, *Physics Reports*, 613, **2016**, 1-20.

[35] A. Kerber, E.A. Cartier, Reliability challenges for CMOS technology qualifications with hafnium oxide/titanium nitride gate stacks, *IEEE Transactions on Device and Materials Reliability*, 9, **2009**, 147-162.

[36] B.H. Lee, L. Kang, R. Nieh, W.-J. Qi, J.C. Lee, Thermal stability and electrical characteristics of ultrathin hafnium oxide gate dielectric reoxidized with rapid thermal annealing, *Appl. Phys. Lett.*, 76, **2000**, 1926-1928.

[37] O. Renault, D. Samour, D. Rouchon, P. Holliger, A.-M. Papon, D. Blin, S. Marthon, Interface properties of ultra-thin HfO 2 films grown by atomic layer deposition on SiO 2/Si, *Thin Solid Films*, 428, **2003**, 190-194.

[38] E.P. Gusev, C. Cabral, M. Copel, C. D'Emic, M. Gribelyuk, Ultrathin HfO2 films grown on silicon by atomic layer deposition for advanced gate dielectrics applications, *Microelectron. Eng.*, 69, **2003**, 145-151.

[39] K. Kim, G.S. Park, Landscape for semiconductor analysis: Issues and challenges, in: 18th IEEE International Symposium on the Physical and Failure Analysis of Integrated Circuits (IPFA), **2011**, pp. 1-9.

[40] K. Kolanek, M. Tallarida, D. Schmeisser, Height distribution of atomic force microscopy images as a tool for atomic layer deposition characterization, *J. Vac. Sci. Technol.*, 31, **2013**, 01A104.

[41] D. Weibel, S. Wong, N. Lockyer, P. Blenkinsopp, R. Hill, J.C. Vickerman, A C60 primary ion beam system for time of flight secondary ion mass spectrometry: its development and secondary ion yield characteristics, *Analytical Chemistry*, 75, **2003**, 1754-1764.

[42] A. Brunelle, D. Touboul, O. Laprévote, Biological tissue imaging with time-of-flight secondary ion mass spectrometry and cluster ion sources, *Journal of Mass Spectrometry*, 40, **2005**, 985-999.

[43] J.S. Becker, U. Breuer, H.-F. Hsieh, T. Osterholt, U. Kumtabtim, B. Wu, A. Matusch, J.A. Caruso, Z. Qin, Bioimaging of metals and biomolecules in mouse heart by laser ablation inductively coupled plasma mass spectrometry and secondary ion mass spectrometry, *Analytical chemistry*, 82, **2010**, 9528-9533.

[44] M.K. Passarelli, N. Winograd, Lipid imaging with time-of-flight secondary ion mass spectrometry (ToF-SIMS), *Biochimica et Biophysica Acta (BBA)-Molecular and Cell Biology of Lipids*, 1811, **2011**, 976-990.

[45] J.S. Fletcher, J.C. Vickerman, N. Winograd, Label free biochemical 2D and 3D imaging using secondary ion mass spectrometry, *Current opinion in chemical biology*, 15, **2011**, 733-740.

[46] K. Shen, D. Mao, B.J. Garrison, A. Wucher, N. Winograd, Depth profiling of metal overlayers on organic substrates with cluster SIMS, *Analytical chemistry*, 85, **2013**, 10565-10572.

[47] M.K. Passarelli, J. Wang, A.S. Mohammadi, R.l. Trouillon, I. Gilmore, A.G. Ewing, Development of an organic lateral resolution test device for imaging mass spectrometry, *Analytical chemistry*, 86, **2014**, 9473-9480.

[48] J. Zhao, X. Zhang, C.R. Yonzon, A.J. Haes, R.P. Van Duyne, Localized surface plasmon resonance biosensors, **2006**.

[49] A. Pimpin, W. Srituravanich, Review on micro-and nanolithography techniques and their applications, *Engineering Journal*, 16, **2012**, 37-56.

[50] C. Wu, T.G. Lin, Z. Zhan, Y. Li, S.C. Tung, W.C. Tang, W.J. Li, Fabrication of all-transparent polymer-based and encapsulated nanofluidic devices using nano-indentation lithography, *Microsystems & Nanoengineering*, 3, **2017**, 16084.

[51] X. Duan, Y. Huang, Y. Cui, J. Wang, C.M. Lieber, Indium phosphide nanowires as building blocks for nanoscale electronic and optoelectronic devices, *Nature*, 409, **2001**, 66.

[52] L. Pan, Y. Park, Y. Xiong, E. Ulin-Avila, Y. Wang, L. Zeng, S. Xiong, J. Rho, C. Sun, D.B. Bogy, Maskless plasmonic lithography at 22 nm resolution, *Scientific reports*, 1, **2011**, 175.

[53] Y. Chen, A. Pepin, Nanofabrication: Conventional and nonconventional methods, *Electrophoresis*, 22, **2001**, 187-207.

Chapter 2 Development of external automation stage for LN-AFM

2.1 Configurations of LN-AFM

Unlike industrial automated AFM which performs full wafer inspections, AFM equipment normally used in the research field aims at measuring the limited surface area of an ultrathin film or variations of nanostructures. Thus, it is not obligatory to install a stage for long distance transportation. For this reason, all mechanical drives, including the movable stage, are removed to construct a robust hardware configuration for low-noise atomic force microscope (LN-AFM).

In order to reduce the mechanical noise, the LN-AFM adopted minimized noise sources by eliminating motion in the sample holder. In addition, the XY and Z scanners were separated to eliminate coupling effect between scanners when measuring CD. The Z scanner (P-010.00H, Physik Instrumente, Germany) is a stack-type scanner that ensures high mechanical stability and positional accuracy. The SNR of the position-sensitive photo diode sensor (PSPD) was improved by separating the heat sources. For this purpose, a low-coherence and low-noise infrared ray (IR, ~ 850 nm), a super-luminescent diode, and an integrated type of CCD were used in the bounce path of the laser beam. The root-mean-square (RMS)

noise of the LN-AFM is as low as 35 pm. However, conversely, in order to give multi-functional tasks to the LN-AFM such as indentations, CD measurements, inspections for certified standard samples, and so on, an external stage capable of mid-range position movement is required.

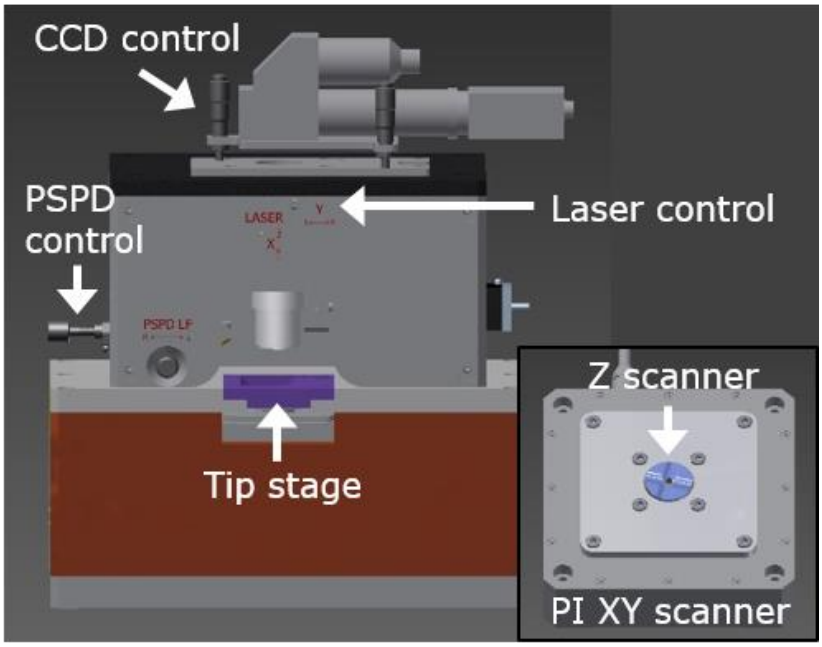

Figure 2.5 CAD image of the LN-AFM. (inset) PI XY scanner for fine positioning.

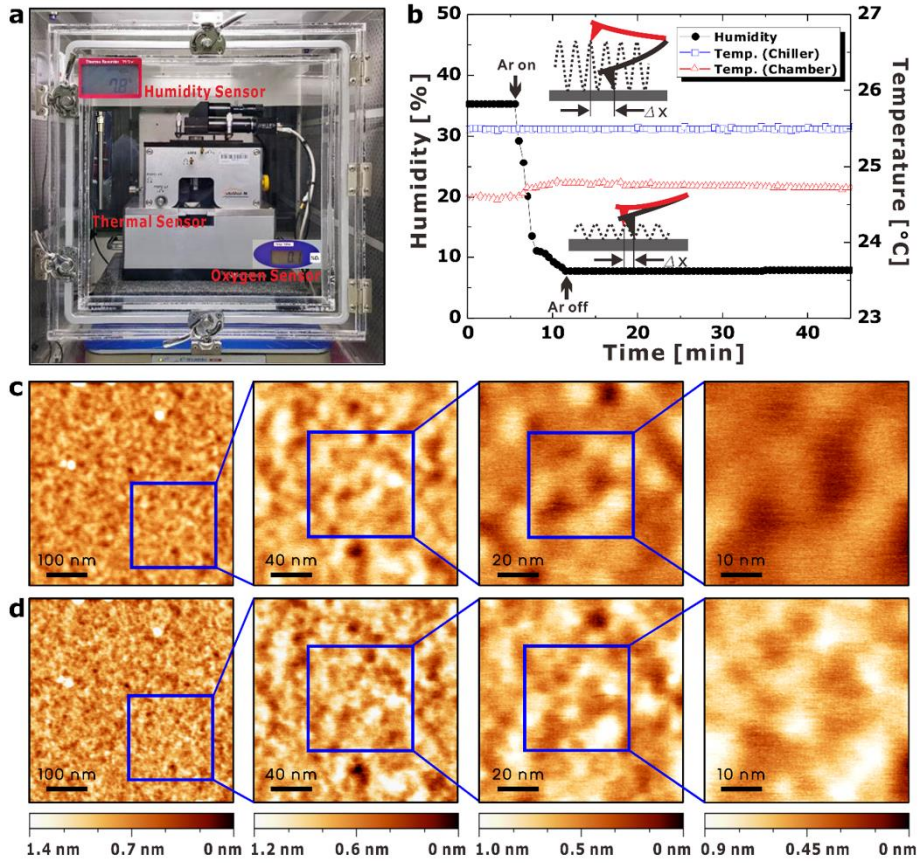

Figure 2.6 (a) LN AFM system equipped with humidity, thermal, and oxygen sensors. The oxygen sensor is used for safety purpose. (b) Plot of the humidity and temperatures in the AFM measurement environments. (c) AFM images of HfO_2 film at a relative humidity of 35%. The RMS roughness is 0.13 nm at a 500 nm FOV. (d) AFM images of HfO_2 film at a low humidity level of less than 10%. The RMS roughness is 0.15 nm at a 500 nm FOV at a position identical to that in panel (c).

2.2 Development of independent external stage

2.2.1 Configurations of the external stage

In this section, the development of an independent mid-range stage for LN-AFM is introduced. The external stage is comprised of three external axes and one sample grip and can be used to determine the coarse x-y position of the target sample after millimeters-travel. Fine x-y adjustments are carried out through the PI XY piezo nanopositioning stage of the LN-AFM.

This system includes a computer with custom-made software, a control box, and an external base for the AFM stage. The detail of the external base will be discussed below. A five-axes controller/driver module (TMCM-6212, Trinamic Motion Control GmbH, Hamburg, Germany) was used to operate the step motors (X, Y, Z, gripper, and rotator) and was designed for serial communication based on an RS485 bus between the computer and the control box. The power for the step motors is supplied from the control box, in which the switching-mode power supply (SMPS) produces DC 24 V/4.2 A and DC 12V/ 2.1 A independently from the two types of motors. These step motors (EN AM2224 AV-4.8 (22mm) and EN AM1524 V-6-35 (15mm), Faulhaber, Croglio, Switzerland) were purchased from Faulhaber. They have 24 steps per revolution, which correspond to a step angle of 15 degrees. A CCD

camera (XCAM 1080PHA, ToupTek, China) was used to capture images and was connected to a PC via a USB cable connection. An electromagnet consisting of a bobbin shaft created by winding a 0.3-mm-thick coil served as a sample anchor with which to maintain a nonslip condition. The 500-turn coil was connected to a DC 12V SMPS and heat generation between the interlayers was prevented by inserting a protective film when winding the coil.

There are two kinds of stages. The first is a universal tip cartridge for cantilever loading, and the other is a four-axes stage for the coarse x-y positioning of the sample. Each stage is designed to be inserted into the external base and the LN-AFM equipment.

The external stage consists of three parts: an optical microscope (Olympus SZX7, Japan) to observe the shape of the sample, a gripper to hold the sample and a base to attach or detach the sample holder to/from the electromagnet. The sample gripper is designed for precise control of the vertical and horizontal positions. Three step motors are assigned to the position control stage to adjust the vertical and horizontal positions. The maximum travel distance is 10 mm. A limit sensor is attached to each axis. The major roles of the limit sensor are to set the origin of each axis and to safely operate the gripper within the travel range. The horizontal and vertical limits are 8 mm and 6 mm, respectively. The diameter of the motors is 15

mm and the holding torque is 22 mNm. The resolution of the step motor is 1.3 μm. However, it does not represent the position accuracy for the external stage. We have tested the coarse x-y positioning as shown in next section. The information will show how accurately the external stage positions the sample.

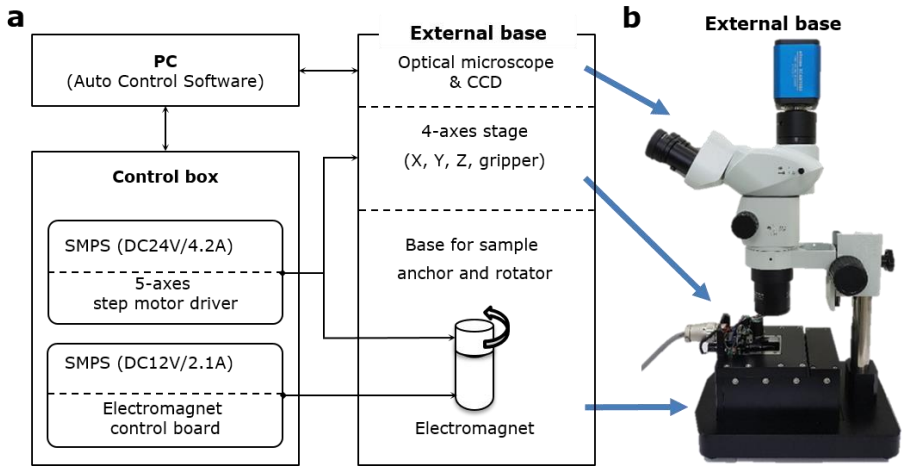

Figure 2.7 (a) Hardware configuration of the external stage system. (b) Photograph of the external base. The external four-axes stage is designed to be compatible with the tip stage of the LN-AFM.

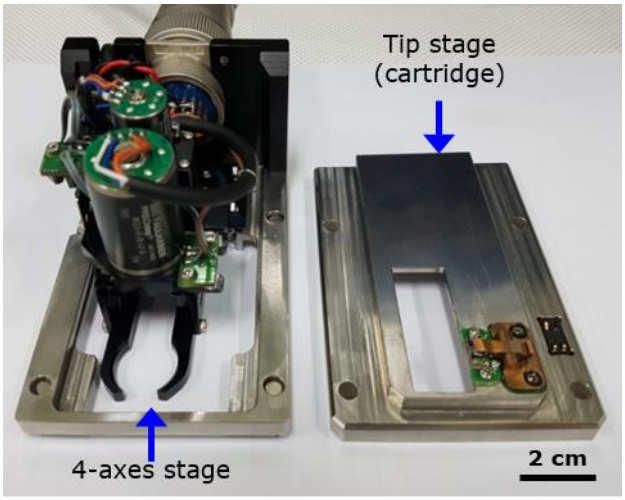

Figure 2.8 Photograph of the external stage for the coarse x-y positioning and the AFM tip stage.

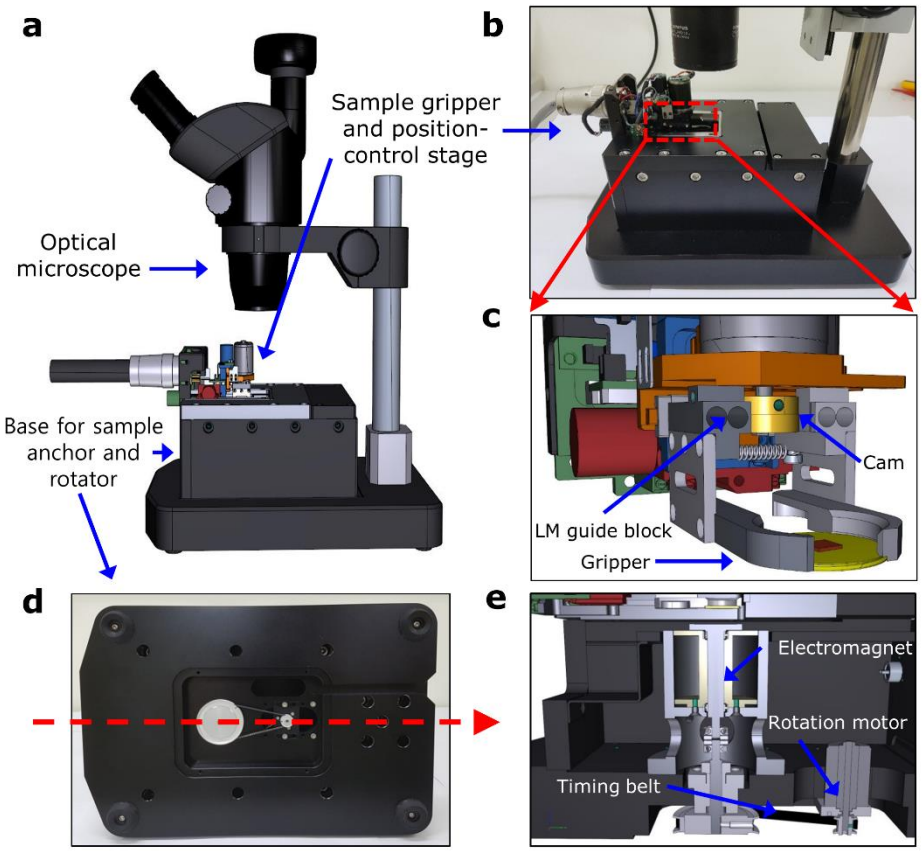

Figure 2.9 (a) Schematic illustration of the external AFM stage. (b) Photograph of the external four-axes stage. (c) Illustration of the sample gripper. (d) Bottom view of the base for the sample anchor and rotator. (e) Cross-sectional view of the base.

2.2.2 Position adjustment method

The position adjustment method for the LN-AFM comprises two steps: coarse and fine control. The developed external four-axes stage moves the sample through mid-distance transport (maximum 10 mm), while fine-tuning of the sample position is performed through the XY piezo nanopositioning stage (P-733.2DD, Physik Instrumente, Germany). The lateral resolution and scan area of the XY piezo nanopositioning stage are 0.1 nm and 30 μm, respectively. During AFM measurements, there is little drift (0.5 nm/min) in the scan range because temperature and humidity are controlled through the environmental chamber.

When moving the sample, the gripper is set to catch the sample. The gripper utilizes a linear motion (LM) guide to open both arms, and a spring is used to fix the sample holder. Linear motion is realized by placing two blocks on the LM guide. The gripper can then be operated by attaching a motor to a cam with a different aspect ratio. A step motor (EN AM2224 AV-4.8 (22mm), Faulhaber, Croglio, Switzerland) is used to rotate the cam, and it has a torque rating of 22 mNm. A sample rotation was achieved by connecting a timing belt to the step motor. The position of the sample can be fine-tuned using a high-magnification microscope, because the rotation resolution is 0.06 degrees.

The method for operating the system comprises three steps: initialization and

recording of the probe position, rotational adjustment and position measurement of the target sample, and mounting of the AFM tip stage and AFM measurements. The details of the operation steps are described in the block diagrams.

The first step is to extract the tip contour and to find the end of the tip. For this purpose, the tip stage is mounted on an external base and an image of the tip is stored using an optical microscope. The software developed in this study identifies the position of the probe and then matches the position and image of the sample to be measured. The location of the probes can be detected by the Canny algorithm using the OpenCV library [1, 2]. After the tip-location information is stored, the tip stage is unmounted.

The second step is to rotate the sample and move to the measurement position. To do this, the sample and the external four-axes stage are loaded onto the external base. When measuring a new position, a tilt correction by sample rotation should be performed in advance and the target position has to be set. In order to repeat the measurement, the sample can be reloaded with automatic rotation correction after sample loading. The position and scaling of the sample can be estimated by comparing the previous image with the current image using the Speeded-Up Robust Features (SURF) algorithm [3]. For position alignment, the location of the probe is determined in advance, after which the target sample is moved to the position of the

probe.

Finally, once the location relative to the probe is recorded through the external stage, it is inserted into the LN-AFM instrument (NanoFocus, Seoul, Korea) and the sample is placed in the same position. The AFM measurement is then performed after the sample is securely mounted in the AFM equipment.

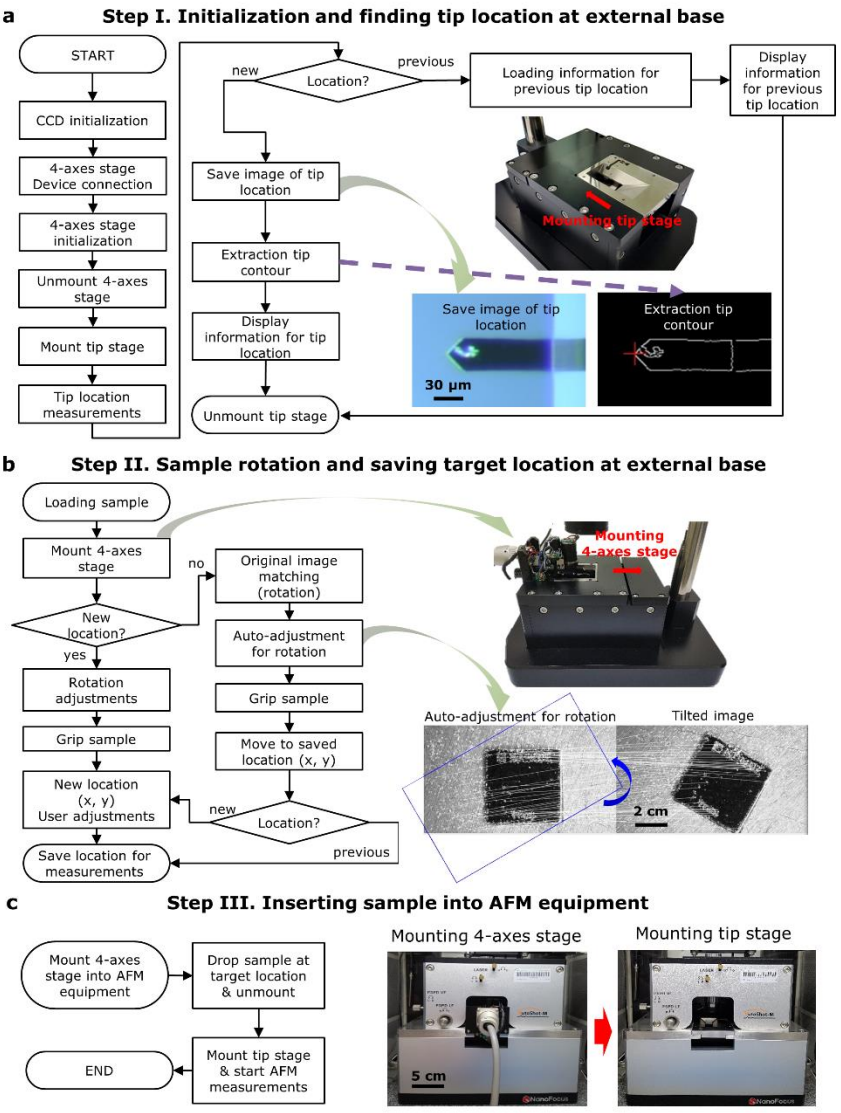

Figure 2.10 Flow chart of the image match process and AFM measurements. (a) Example of picking up the tip contour using the Canny algorithm and recognizing the tip position. (b) Example of position matching with a previously saved image using the SURF algorithm. (c) Mounting process of the external stage.

2.2.3 Position accuracy test

A sample preparation method for the experiments of the mid-distance transportation is as follows. The 4-inch glass substrate was diced to 1 cm × 1 cm. Cross patterns were formed on the glass substrate using a photolithography method. A negative photoresist (DNR-L300-30, Dongjin Semichem Co., Ltd., Seoul, Korea) was used for this fabrication. ID numbers were assigned to each cross, and the pitch between the crosses was 2 mm. Cr/Au (3/17 nm) layers were deposited by an electron beam evaporation method. The sample was immersed in acetone for the metal lift-off process. The surface was rinsed with deionized water and dried in nitrogen gas blow.

The target sample was attached to a circular stainless steel (SUS) substrate using a conductive silver paste. Using the rotation stage mounted on the external base, the tilted angle was adjusted with the baseline shown on the screen. The gripper held the SUS board before moving. Initially, the starting point was recorded and the sample was lifted to a height of 1 mm. The sample was then moved 2 mm in the horizontal direction. The sample was brought into contact with the external electromagnet base. To record the final position, the images of the moved positions were obtained by the microscope. This procedure was repeated 12 times. The location information for each image was analyzed using ImageJ software[4]. As

shown in the figure below, positional inaccuracy after mid-distance travel was about 9.1 μm. The causes of this inaccuracy result from the gripping error, the impact caused by contact with the magnet base, and the operating error of the stepper motor.

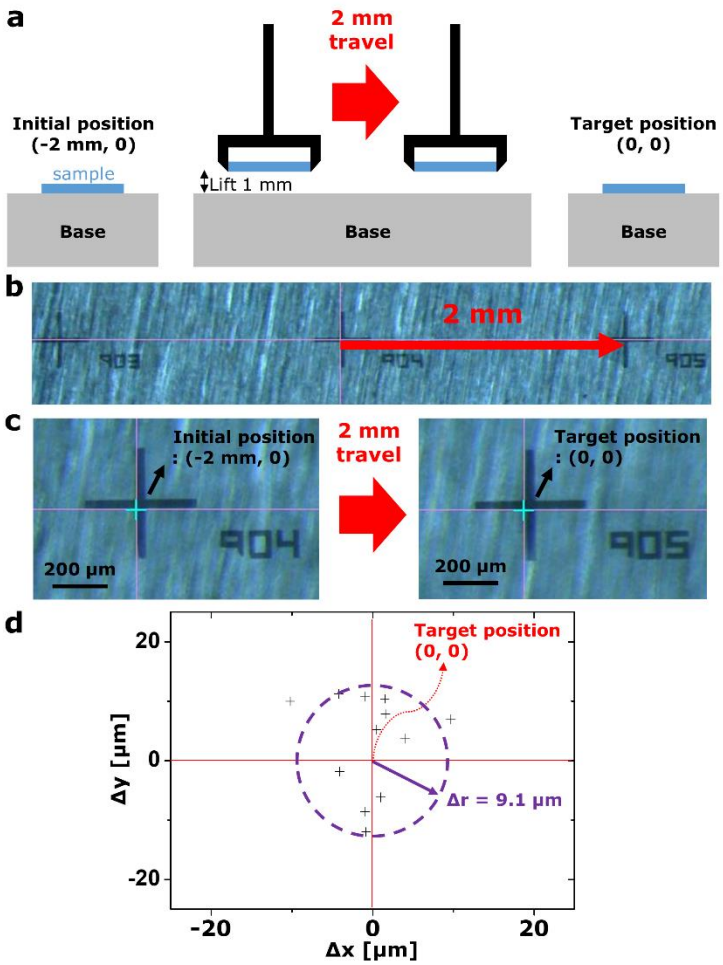

Figure 2.11 A position accuracy experiment for coarse x-y positioning using the external four-axes stage. (a) A schematic diagram of a mid-distance-travel experiment. (b) Microscope image of the cross-marked sample. Cross markers were fabricated by Cr/Au deposition with patterns of 2 mm intervals. (c) Enlarged image of (b). Optical microscope images of the initial and final points during the migration experiment. (d) Results of the position error after 12 repetitions of the experiment.

The coordinates of the cantilever can be changed by an incorrect position of the tip stage, even if the sample is inserted precisely at the desired position by the four-axes outer stage. Therefore, in order to confirm the position accuracy of the tip stage based on the repeatability of the mounting process, the tip location was directly recorded using an indentation experiment[5-7]. For this experiment, a poly-methyl methacrylate (PMMA A4, MicroChem Corp., Westborough, MA, USA) layer was spin-coated onto a glass substrate, after which a thin gold film (10 nm thick) was deposited by an electron-beam evaporator (Ultech Co., Ltd., Daegu, Korea).

In this study, in order to confirm the error of the tip stage, indentation method was used. It might be impractical to use indentation techniques for lots of application. However, when inserting tip cartridges, it is inevitable that the tip position will be loaded differently each time. So the purpose for the indentation techniques is not to find the position of the tip every time. We are trying to estimate the magnitude of the error that occurs when the tip cartridge is loaded. This experiment was possible because the indentation point could represent the measurement position of the tip stage.

Prior to the indentation step to determine the tip positions, the surface of a 20 μm scan area was confirmed. Three point defects were detected, as shown in the figure. Subsequently, an indentation dot was set to the origin using an HDC tip (400

nm long EBD-HAR short probes, Nanotools GmbH, München, Germany), and a 3 × 3 array marker was placed at the upper right corner. Indentation was performed at each tip position while the tip stage was inserted and detached. This procedure was repeated 10 times, and topological images were acquired using the HDC tip that was used for the indentation process. All topological images were processed with WSXM software[8]. Interestingly, all 10 indentation points were distributed within 6 μm and listed in the forward direction with respect to the origin. This is the tip-loading direction.

The position of the tip may be changed each time while repeating loading tips and samples. The position errors of the sample occur in two situations. One is the mounting error of the tip stage and the other is positioning error caused by the external stage. The mounting error of the tip stage was 6 μm and the position error of the external stage was 9.1 μm. Both errors are independent each other and may occur at the same time. In the worst case, the maximum position error under this condition can be about 15 μm. However, even in the worst positioning error, the user can find the desired position of the target patterns which are located at the boundary of the field of view because the maximum field of view for the PI XY scanner is 30 μm (PI XY piezo scanner, P-733.2DD, Physik Instrumente, Germnay, Scan range 30 um,

resolution: 0.1 nm). Therefore, the inaccuracy of the sample position is considered to have only a negligible influence on our measurements.

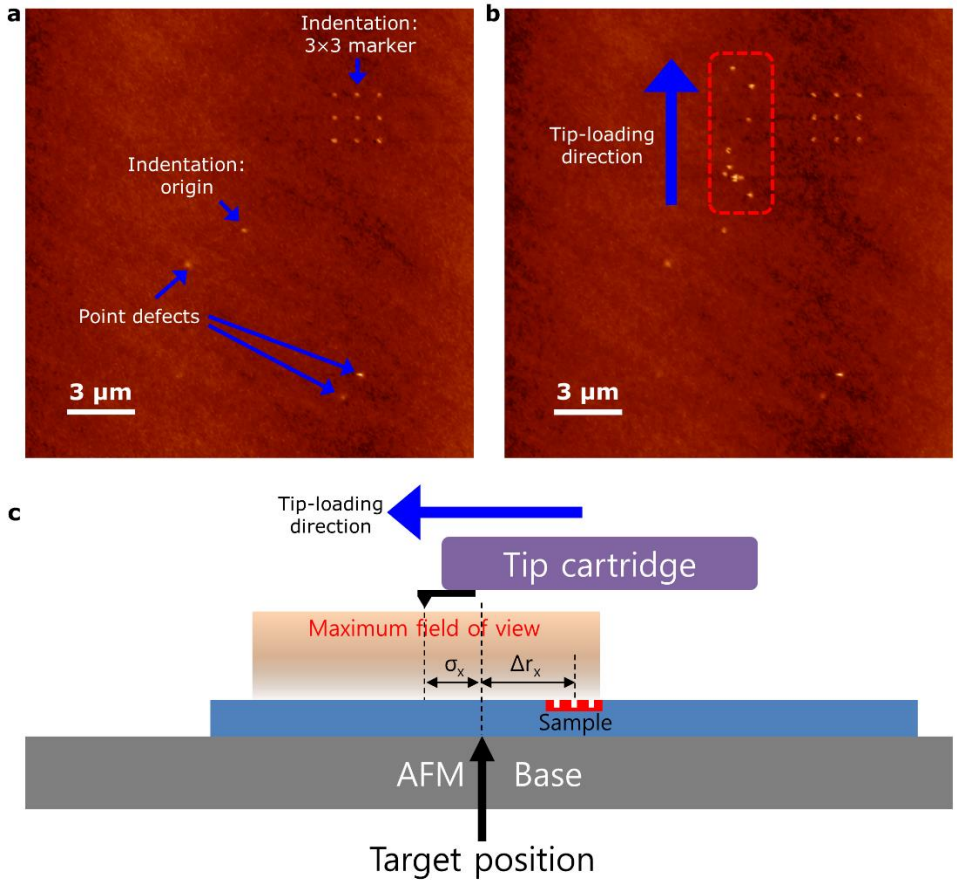

Figure 2.12 Position accuracy of the tip stage as measured by the indentation method: (a) Initial condition (indentation for the origin and marker). (b) Tip positions are expressed by AFM indentation during the mounting and unmounting process of the tip stage. This was repeated ten times. (c) Schematic drawing of maximum position errors. The σx and Δrx represent the mounting error of the tip cartridge and position error of the external stage along the tip-loading direction, respectively. In the worst positioning error, the IVPS patterns are located at the boundary of the field of view.

2.3. Reference

[1] I. Culjak, D. Abram, T. Pribanic, H. Dzapo, M. Cifrek, A brief introduction to OpenCV, in: MIPRO, 2012 proceedings of the 35th international convention, *IEEE*, **2012**, pp. 1725-1730.

[2] Y. Luo, R. Duraiswami, Canny edge detection on NVIDIA CUDA, in: Computer Vision and Pattern Recognition Workshops, 2008. CVPRW'08. IEEE Computer Society Conference on, *IEEE*, **2008**, pp. 1-8.

[3] H. Bay, A. Ess, T. Tuytelaars, L. Van Gool, Speeded-up robust features (SURF), *Computer vision and image understanding*, 110, **2008**, 346-359.

[4] C.A. Schneider, W.S. Rasband, K.W. Eliceiri, NIH Image to ImageJ: 25 years of image analysis, *Nature methods*, 9, **2012**, 671.

[5] J. Gong, D.J. Lipomi, J. Deng, Z. Nie, X. Chen, N.X. Randall, R. Nair, G.M. Whitesides, Micro-and nanopatterning of inorganic and polymeric substrates by indentation lithography, *Nano letters*, 10, **2010**, 2702-2708.

[6] C. Shin, I. Jeon, S. Jeon, Z.G. Khim, Single nanoparticle alignment by atomic force microscopy indentation, *Applied Physics Letters*, 94, **2009**, 163107.

[7] S. Jeon, B. Ryu, W. Jhe, Z.G. Khim, B.I. Kim, Reproducible nanostructure fabrication using atomic force microscopy indentation with minimal tip damage,

Journal of Vacuum Science & Technology B, Nanotechnology and Microelectronics: Materials, Processing, Measurement, and Phenomena, 32, **2014**, 020601.

[8] I. Horcas, R. Fernández, J. Gomez-Rodriguez, J. Colchero, J. Gómez-Herrero, A. Baro, WSXM: a software for scanning probe microscopy and a tool for nanotechnology, *Review of scientific instruments*, 78, **2007**, 013705.

Chapter 3 Industrial applications using the LN-AFM with the external stage

3.1 Industrial demands

The demand for mobile devices, the internet of things (IoT), and artificial intelligence (AI) has increased dramatically, and the semiconductor industry is also making efforts to expand supply. In particular, with the emergence of high-capacitance and low-power devices in the semiconductor industries, lithographic patterns for next-generation semiconductors have become increasingly complicated, and the thicknesses of these films have been reduced from a few nanometers to the subnanometer range [1-3]. Given that the production yield of semiconductor devices during in-line processing should be improved in the near future, examining not only the thickness of these thin films but also the 3D surface information is necessary.

As the development of the Fin-FET structures and NAND devices has accelerated, there has been a demand to observe the 3D shapes. In a three-dimensional structure with a high aspect ratio, many attempts are made to probe the sidewall of the vertical structures to check the roughness of the sidewall or to estimate the critical dimension. However, in the conventional method, image distortion may occur when observing high aspect 3D structures. Therefore, an

appropriate tip and operating mode should be selected for the inspections of the nanostructures.

Another industrial concern is management of ultrathin films below the 0.5-nm equivalent oxide thickness. As new insulating materials and multilayer techniques are introduced, a thickness metrology for ultrathin films is becoming significant. Thus, new industrial criteria are required to enhance production yield and stable process control through reliable inline metrology together with an increasing production scale. Thickness metrology now requires quantitative methods for surface topology and interface effects between each multilayer film as well as thickness measurement. For that purpose, roughness metrology through nanometer- or angstrom-level process control will reinforce the thickness metrology because the roughness of the ultrathin films directly impacts the local thickness of the films, which can affect the performance and lifetime of the devices.

For these purposes, the AFM is the best metrological method to quantify the properties of semiconductors and to analyze the various shapes of the surface structures by directly scanning them in a nondestructive manner [4-6].

3.2 Critical dimension measurements

3.2.1 Vector approach probing method

The 3D AFM technique aims at versatile measurement outcomes, such as the height, width, and sidewall profile. In current inline metrology, automated CD-AFM acquires images via the dithering method. In this method, when measuring the sidewall of the trench pattern, the enough pitch between the patterns, which is about twice as large as the tip head, should be secured. As the width of the patterns become smaller, the demands for the use of small CD tips are increasing. Moreover, the tendency of sticking to the sidewalls must be solved [7-9]. The measurement strategy of the low noise atomic force microscope (LN-AFM) was sourced from a method in the literature known as the vector approach probing (VAP) method, which was developed by German Physikalisch Technische Bundesanstalt researchers for CD measurements [10, 11]. Although this method is relatively slow and requires accurate measurement positions during CD measurements, it is capable of measuring at narrow trenches where the tip size is approximately the total width of the pattern.

3.2.2 Advantages and limitations

The advantages of the VAP method is that the measurements can be made in narrow trenches where the tip head size is close to the total width of the pattern. Moreover, by obtaining the image directly through the point-contact, tip wear can be reduced with accurate side-pattern images. Limitations of our approach is that the speed of the measurement is slow. The accurate location for the measurement is strictly required.

3.2.3 CD measurement using vertical structure

The sidewalls of the improved vertical parallel structure (IVPS) and the calibration grating (TGX1) samples were then examined by precisely aligning the position of the CD tip. From these experiments, the capabilities of the external stage are indirectly verified.

A CDR30-EBD tip (Nanotools GmbH, München, Germany) for the sidewall measurements of the IVPS100 reference sample was used. The reason for choosing a small-head CD tip is that there is a demand for measuring trench patterns with a narrow width in the current semiconductor industry. As depicted in Fig 6a, the tilt compensation angle (θ) of the tip is 13° (± 1°) and the total width (d) of the tip head

is 30 nm. The vertical edge height (VEH) and the effective length (l) are 10 nm (<15 nm) and 150 nm, respectively. The length of the overhang (OH) structure is 8 nm (5~10 nm). The force constant of the cantilever is 40 N/m (± 20 nm).

The pitch of the IVPS100 trench patterns is 500 nm ± 10 nm, and the depth is approximately 1 μm. The IVPS100 (Team Nanotec GmbH, Germany) sample, which has steep sidewalls, is commonly used in CD measurements [8, 12-14]. To measure the side of this sample, the sample orientation should be adjusted to be perpendicular to the direction of the tip. Otherwise, the tip will be broken or the measurement will be distorted due to tip wear and incorrect positions. Therefore, the CD measurements can inform whether external stage is working properly.

The developed stage enabled us to measure the pattern accurately at the desired position. The measurements were performed by the VAP method. Two repeated-measurement profiles are shown in Fig. 6c. The sidewall should ideally be formed vertically. However, as a result of the measurement, it seems that the sidewall has a slope. This is because the CDR30-EBD tip has a short effective length. Hence, the slope must be calculated through repetitive measurements.

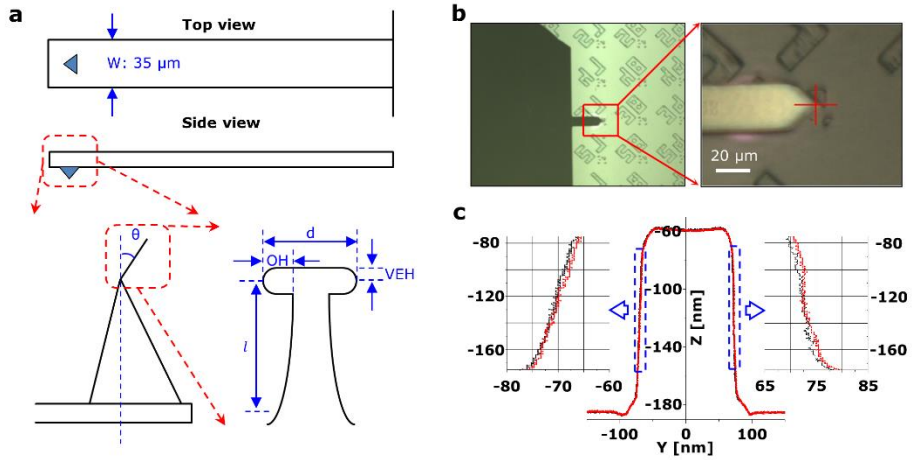

Figure 3.13 (a) Top view and side view of the CDR30-EBD tip. (b) Tip stage loaded at the desired position to scan the trench patterns of the IVPS100. (c) Measured IVPS100 pattern. Two profiles are shown in the plot. Details of both sidewalls are shown in the inset.

Only limited depth profiles (up to 125 nm deep) were recorded using a software function because the depth of the trench patterns was greater than the effective length of the tip. The CD measurement method and the angle calculation method for the trench patterns are as follows. The 30% of upper and lower data was excluded from the CD and angle calculations, following a method developed previously [11]. That is, the middle CD values were calculated. The average horizontal position of the first trench wall is denoted by Y1, and the average horizontal position of the second wall is denoted by Y2. The middle CD value is then equal to mean (Y2) - mean (Y1). The angle values were calculated through the first order linear fitting of the selected data, and the angle was found through the arctan (slope) value.

The sidewall measurements were repeated 30 times at the same position. The mean value and the standard deviation were 141.9 nm and 0.6 nm, respectively. For reproducibility measurements, both the sample and tip cartage were reloaded 10 times. As a result, the average value of the CD measurements was 142 ± 0.8 nm, which is similar to the repeatability results. Furthermore, the angles of the left and right walls were calculated to be 86 ± 0.2 ° and 87.1 ± 0.1 °, respectively.

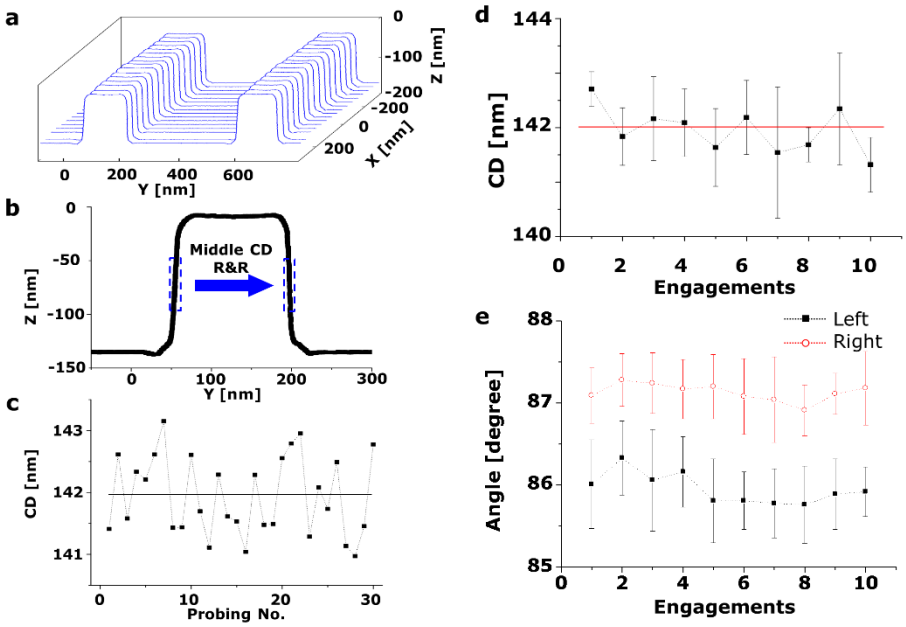

Figure 3.14 (a) Reconstructed 3D profiles of the IVPS patterns. (b) Example of the CD repeatability and reproducibility (R&R) measurement. (c) Results of the CD measurements, repeated 30 times at the same position. Solid (black) line shows the mean value (141.9 nm). (d) Reproducibility measurements for 10 engagements. Solid (red) line exhibits the mean value (142 nm). (e) Calculated sidewall angles of the IVPS sample for 10 engagements. (left and right sidewalls)

3.2.4 Tip wear test

After the 30-times-repeated CD measurements, we also investigated a calibration grating (TGX1, NT-MDT Co., Moscow, Russia) sample, which has a chessboard-like array of square pillars with a sharp undercut pattern [15]. By doing so, we were able to confirm the wear of the CD tip. This experiment is another way to check the performance of the external stage. The length of the OH structure of the CD tip after the repeatability measurements can be estimated by measuring the undercut structure of the TGX1. The calculated mean value of the tip-overhang from the TGX1 data was 7.27 ± 1.03 nm which is still close to the OH value indicated by the specification sheet.

The external stage developed here shows successful matching the positions of the tip and the sample using the custom-made software. In addition, we obtained good position accuracy for the external stage and the tip stage through the reproducibility experiments. Hence, we successfully measured the CD value using the external stage at precise locations, and the average values for 30-times-repeated measurements and 10-times-reproduced CD values were 141.9 ± 0.6 nm and 142 ± 0.8 nm, respectively. Finally, we confirmed that the tip wear was minimized by measuring an undercut TGX1 sample. We expect this study to be helpful in the

inspection of semiconductor manufacturing [16, 17], the large-area indentation patterning [18], the study of nano-bio materials [19, 20], and the surface analysis of thin films using AFM [21-23].

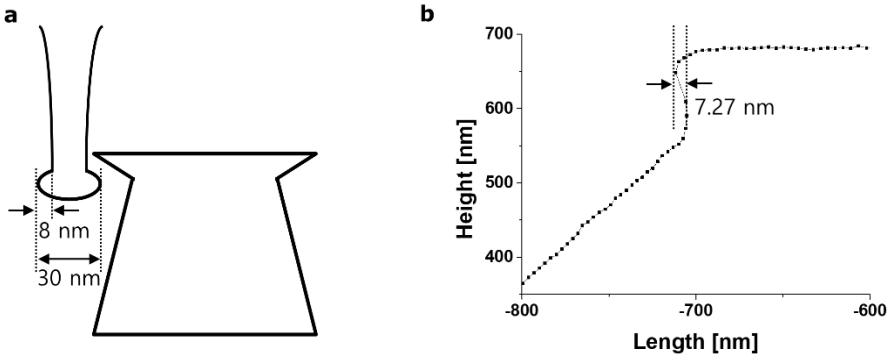

Figure 3.15 (a) Schematic illustration of the undercut measurements of the TGX1 sample using the CD tip. (b) Plot of the measured sidewall of the TGX1 sample.

3.3 Critical roughness measurements

3.3.1 Fabrication of ultrathin film using atomic layer deposition

A hafnium oxide ($HfO_{2)}$ layer (3 nm) was deposited onto the surface-treated Si substrates using ALD equipment (Nano-ALD2000; IPS, Pyeongtaek, Korea) because the thickness is corresponding to the 0.5-nm equivalent oxide thickness Tetrakis(ethylmethylamino)hafnium (TEMAHf) and ozone (O_3) were used to form the hafnium oxide layer at 350℃. The gas pressure was 0.7 Torr. In order to check the optimal conditions of the ALD process, different cycles of the process were conducted. From the cross-sectional TEM images, it was confirmed that the target thickness was well constructed. The high-resolution transmission electron microscopy (TEM) image of the hafnium oxide film was taken with a JEM-2100F (JEOL, Tokyo, Japan). The thickness of the HfO2 film was calculated to be approximately 3 nm by DigitalMicrograph (Gatan, Pleasanton, CA, United States) software.

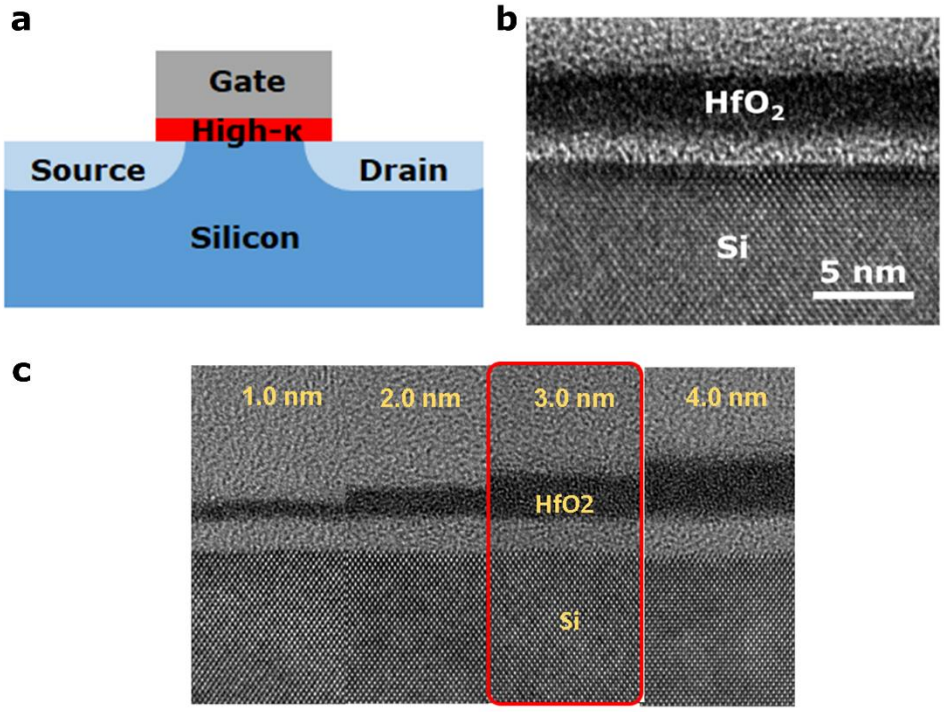

Figure 3.16 (a) MOSFET structure (b) Dielectric layer deposition (3 nm thick) on Si substrate. (c) Different cycles of hafnium oxide films fabricated by ALD. EOT 0.5 nm thickness is corresponding to the 3 nm thick hafnium oxide film.

3.3.2 Reliability of surface roughness measurements

The candidates of the noise sources of the LN AFM are the equipment itself and the environment. The noise of the facility can be managed with a very constant level, and the measurements using the LN AFM were tried to prevent the external environmental influences. Thus, we measured five different sites (upper, lower, left, right, and center position) of the mass produced hafnium oxide film to estimate the uncertainty for the roughness measurements. In addition, we obtained the reliable measurement values from z-piezo value using a tilt stage of LN-AFM (not shown here for the tilt stage). According to the Guide to the Expression of Uncertainty in Measurement (GUM), the combined uncertainty (R_2) can be expressed by below relation.

$$u_c(R_2) = \sqrt{R_1^2 * u^2(K) + \overline{K^2}\{u^2(R_a) + u^2(R_b) + u^2(R_c) + u^2(R_d)\}} \quad (3.1)$$

where $u(K)$ is the calibration coefficient, R_a is the uncertainty of caused by the repeatability measurement, R_b is the uncertainty of caused by the non-uniformity (5 different sites) of specimen, R_c is the uncertainty of instrument noise of z-feedback without x-y motion, R_d is the uncertainty of tip wearing during measurement, R_1 is the average value of RMS roughness measurement, and $\overline{K}$ is the average calibration

coefficient of the instrument.

The custom-built LN AFM system used here which was developed at Korea Research Institute of Standards and Science. The temperature (22.3 ± 0.1℃) of the LN-AFM system can be controlled by circulating temperature-controlled liquid. An ultrathin HfO2 surface was inspected in tapping mode using a high-density carbon probe (SuperSharpStandard-NCHR; Nanotools, Germany) with a normal probe radius of ~ 3 nm and a cantilever spring constant of 40 N/m. The tip diameter of the manufacturer specifications is below 10.0 nm. The cantilever was oscillated at 5.28 nm (free-air amplitude) with a Q-value of 537. The set point of the distance between the probe and the sample was 4.4 nm. When the AFM probe was engaged on the sample, we kept the set point at 7 nm for a wide separation distance to reduce or prevent damage to the probe. The probe was then slowly moved toward the sample in 0.1 nm steps with a large proportional and integral gain factor.

Table 3.1 Summary of uncertainty

Source of uncertainty	**Contribution of each uncertainty source**
Calibration coefficient, u(K)	0.012
Repeatability, u(R_a)	0.003 nm
Non-uniformity, u(R_b)	0.003 nm
Instrument noise, u(R_c)	0.035 nm
Tip wearing, u(R_a)	0.003 nm
u(R_2)	0.036 nm

3.3.3 Interfacial effects using roughness scaling method

A wet etch process was used to make roughened silicon (Si) substrates. The surface roughness was regulated by changing the dipping time in a buffered oxide etchant (BOE) solution. In order to examine the spatial resolution by using LN-AFM in a range of a few nanometers, the roughness of the Si surface was increased until the maximum peak-to-valley value (Rt) approached 3 nm. This process is designated as the “roughness scaling method”.

When determining the scaling range, the Rq value of the sample subjected to the O2 plasma process on the bare Si substrate was designated as the minimum point. The Rq value of the bare Si substrate was 0.15 nm and increased to 0.17 nm after the O2 plasma treatment. The maximum roughness was set to Rq = 0.36 nm because the maximum peak-to-valley values reached the film thickness when dipped in the BOE solution for more than 7.5 minutes.

The samples that did not undergo the BOE process are denoted as “0 min”. An oxygen plasma treatment was conducted after surface etching because the hydrogen-terminated Si surface shows poor nucleation and forms a nano-island morphology during the atomic layer deposition (ALD) process [24-28]. The surfaces of each of the samples were measured with the LN AFM instrument before and after the hafnium oxide deposition process. The

piranha-treated sample was named “Piranha” instead of BOE etch process. To do this, Si wafers were immersed in a piranha solution (a 3:1 mixture of H2SO4 and H2O2) for 30 min and rinsed with deionized water. Oxygen plasma was implemented at a pressure level of 100 mTorr for 90 sec. Subsequently, a hafnium oxide film sample with a thickness of 3 nm was deposited onto the Si surface. The other samples were immersed in BOE solution at different times. The AFM images of the underlayers (SiO2) were measured 5 times for each sample after the oxygen plasma. The AFM images of the overlayers (HfO2) for each sample were measured 5 times at different points after the ALD process.

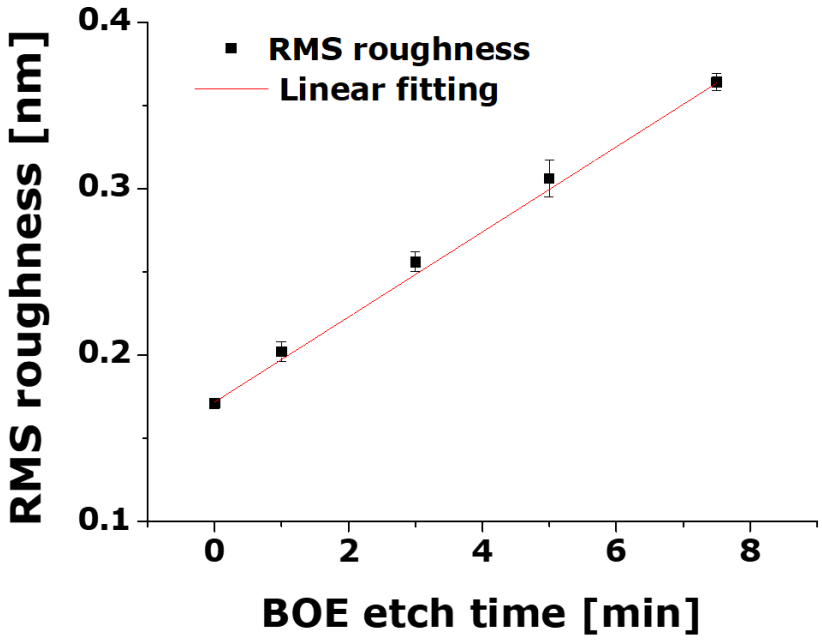

Figure 3.17 This plot shows how to determine the underlayer roughness range in the roughness scaling method.

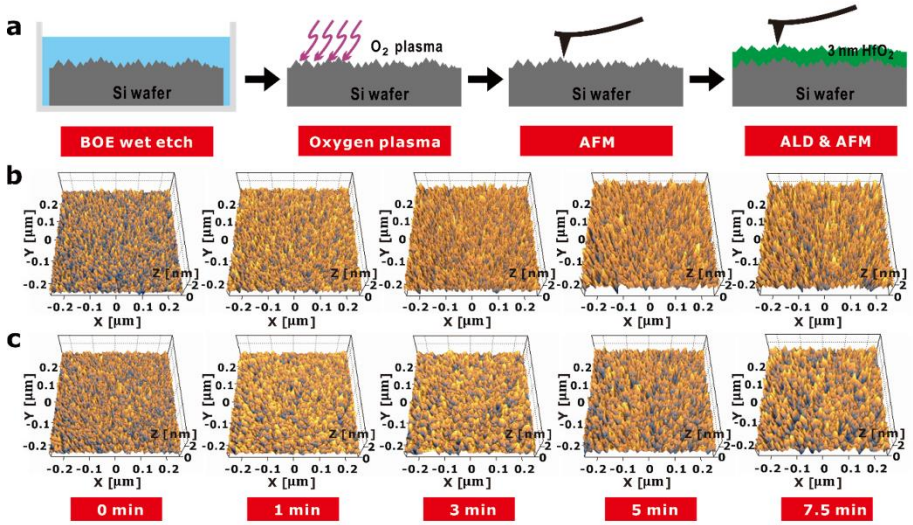

Figure 3.18 (a) Schematic illustration of the roughness scaling method. Roughness scaling (Si substrates) was carried out using a BOE solution with different dipping times. (b) Representative AFM images of roughened silicon surfaces taken after oxygen plasma treatments. (c) AFM images of hafnium oxide surfaces after atomic layer deposition (3 nm in thickness).

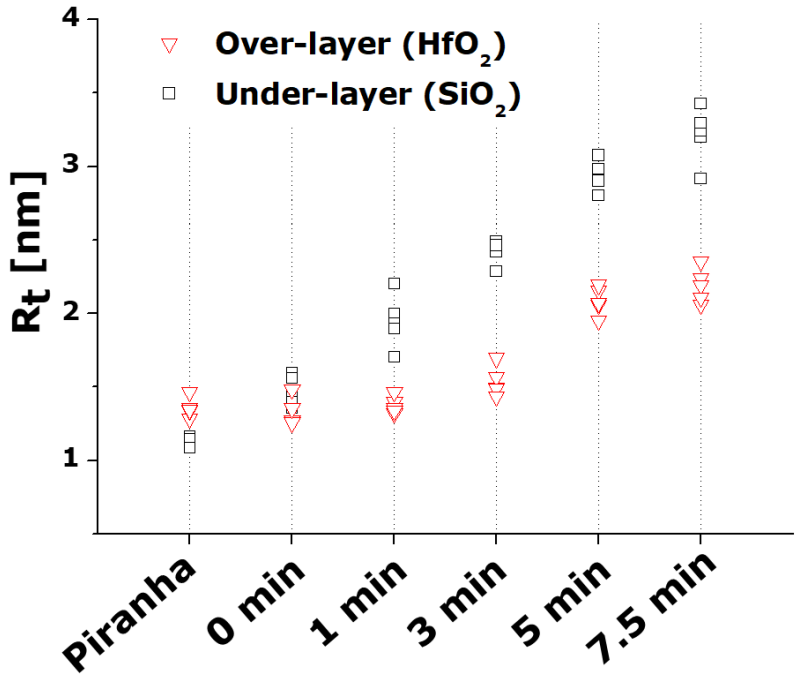

Figure 3.19 Maximum peak-to-valley (Rt) distributions of AFM images for 5 measurements. Each measurement was taken before and after the ALD process. The black square data represent the Rt values of silicon oxide surface. The red triangle data show the Rt values of hafnium oxide films.

3.3.4 Definition of critical roughness

In order to determine the difference between the initial and final states of the surface roughness, the height distributions are overlapped in the plots. The parameters are extracted from these distributions. The arithmetic average of the roughness, the RMS roughness, and the distance between the highest peak and the lowest valley are denoted by R_a, R_q, and R_t, respectively. The result can be distinguishable into two groups. On the relatively smooth substrates, there is no significant effect on the roughness of the HfO_2 overlayer. It can be explained as the smoothing phenomenon during ALD process that was also observed in other studies [29, 30]. However, the RMS roughness of the HfO_2 overlayer is dramatically increased when the R_t values of the rough silicon surface approaches the thickness of the hafnium oxide film. This phenomenon is significantly related to the conformal growth of the ALD process since the surface variations are sufficiently high [31, 32]. In other words, the final roughness is less affected by the underlayer (Si substrates) unless the R_t values of the Si substrates match the thickness of the HfO_2 film. Thus, we can determine the critical roughness based on the experimental data. Two linear fits were conducted to find each slope and intercept. The parameters of the first linear fit data were calculated by selecting the five lowest data values. The parameters of the second fit data were extracted from the three highest data values.

The critical roughness can be determined from the intersection between the two linear fits, as described by the following equations:

$$\mathrm{CR_{over}}|_{t=3\ nm}^{HfO_2} = \frac{b_1 - \alpha b_2}{1-\alpha}, \qquad (\alpha \equiv \frac{a_1}{a_2}) \qquad (3.2)$$

$$\mathrm{CR_{under}} = \frac{1}{\beta}(b_1 - b_2), \qquad (\beta \equiv a_2 - a_1) \qquad (3.3)$$

where t is the thickness of the hafnium oxide film, a_1 and b_1 are correspondingly the slope and the intercept extracted from the first linear fitting function, and a_2 and b_2 are likewise the slope and the intercept of the second linear fitting function. The finally estimated CR value of the HfO_2 overlayer in this dielectric system was 0.18 nm while the CR value of the underlayer was 0.27 nm. Moreover, in order to verify the effectiveness of the CR, we measured the leakage current through the metal-insulator-metal (MIM) diode structure [33, 34]. A highly doped Si wafer was used for the substrates of the MIM diodes. In the case of highly doped Si wafers, it took a long time to adjust the roughness by the BOE wet etching, so the roughness was controlled by the KOH wet method. The control sample was subjected to O_2 plasma treatment without etching, and the hafnium oxide film (3-nm-thick) was fabricated by ALD method. Subsequently, the aluminum film (50-nm-thick) was deposited by a thermal evaporator to complete the MIM structure. The diameter of the aluminum pad metal is 500 μm. A two-probe system was used

for the current measurement and the average value was evaluated through 20 different devices. The IV plot shows minimum, median, and maximum values among 20 devices, and is drawn with different Si roughness. As shown in the logarithm plot, almost all devices show constant current before the CR, whereas the current of the device with a larger roughness than the CR is increased. Therefore, the CR value defined by the simple method in this study proved to be effective. Although the CR value in this experiment is not an absolute criterion for all hafnium oxide films, we believe that the proposed method will be useful for establishing an industry standard CR.

Table 3.2 Roughness information for surface control samples at a 500 nm FOV

	Surface	R_a [nm]	R_q [nm]	R_t [nm]
Piranha	Silicon oxide	0.11	0.14	1.15
	Hafnium oxide	0.12	0.16	1.34
BOE 0 min	Silicon oxide	0.14	0.17	1.47
	Hafnium oxide	0.13	0.17	1.35
BOE 1 min	Silicon oxide	0.16	0.20	1.93
	Hafnium oxide	0.14	0.17	1.36
BOE 3 min	Silicon oxide	0.21	0.27	2.45
	Hafnium oxide	0.14	0.17	1.49
BOE 5 min	Silicon oxide	0.25	0.32	2.98
	Hafnium oxide	0.19	0.24	2.07
BOE 7.5 min	Silicon oxide	0.28	0.36	3.24
	Hafnium oxide	0.22	0.28	2.19

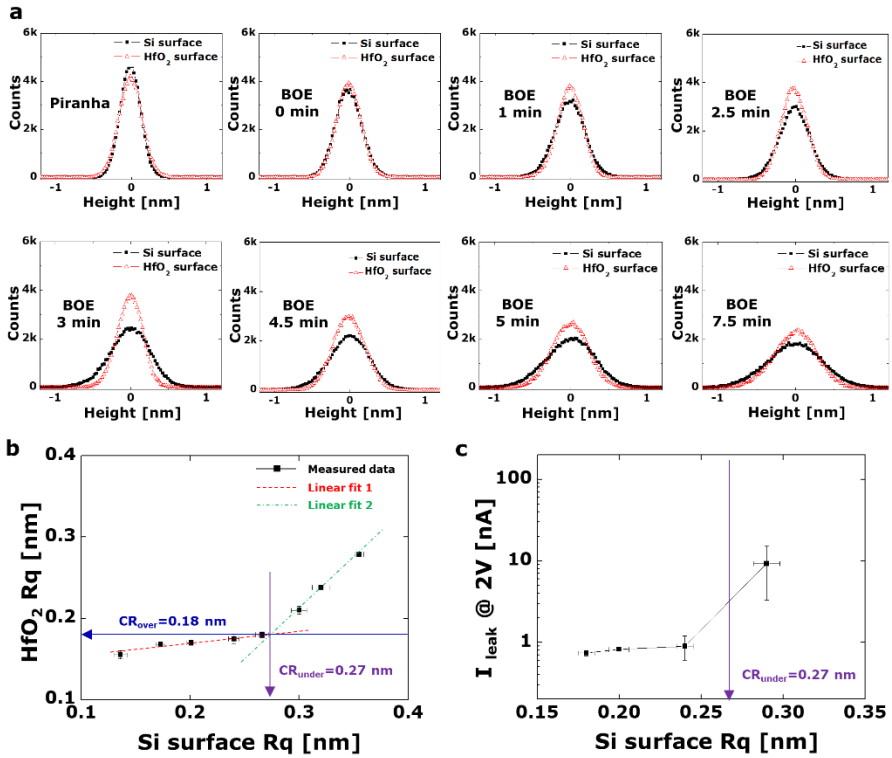

Figure 3.20 (a) Histograms of the height distributions of each AFM image at 500 nm FOV. (b) RMS roughness of a silicon surface before the ALD process vs. a hafnium oxide surface for five measurements. The first linear fit data (slope 0.13, intercept 0.14 nm) was extracted from the four lowest data values. The second fit data (slope 1.24, intercept -0.16 nm) was extracted from three highest data values. (c) Current at 2 V from the MIM diode structure with different RMS roughness of the Si substrate.

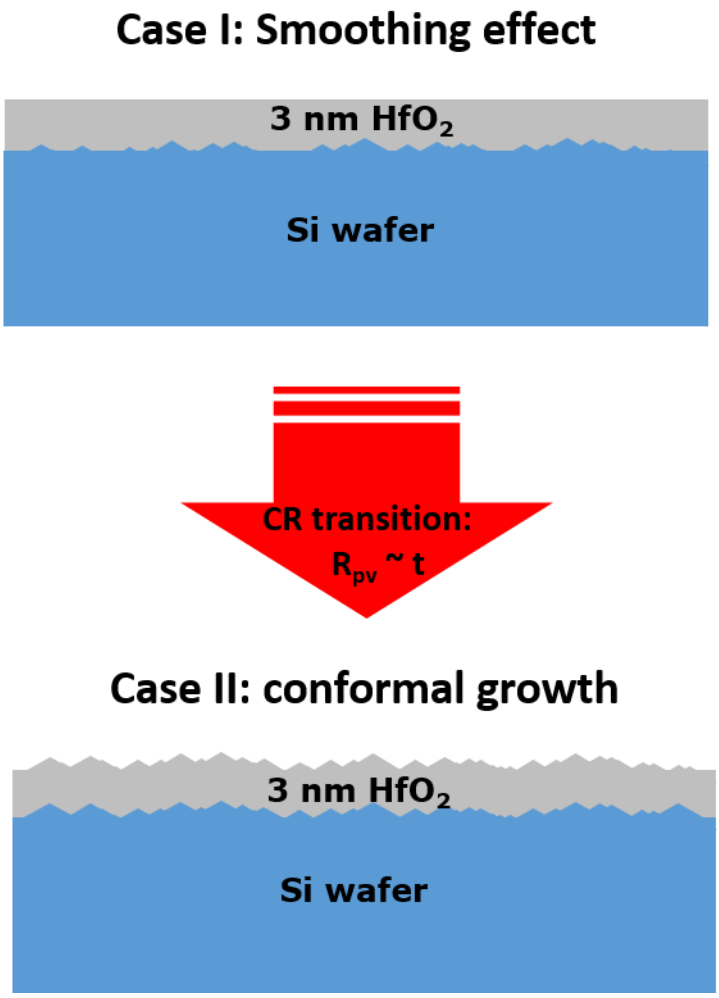

Figure 3.21 Conceptual definition of the critical roughness.

3.3.5 Effectiveness of the critical roughness

In order to verify the effectiveness of the CR, we measured the leakage current through the metal-insulator-metal (MIM) diode structure [33, 34]. A highly doped Si wafer was used for the substrates of the MIM diodes. In the case of highly doped Si wafers, it took a long time to adjust the roughness by the BOE wet etching, so the roughness was controlled by the KOH wet method. The control sample was subjected to O_2 plasma treatment without etching, and the hafnium oxide film (3-nm-thick) was fabricated by ALD method. Subsequently, the aluminum film (50-nm-thick) was deposited by a thermal evaporator to complete the MIM structure. The diameter of the aluminum pad metal is 500 μm. A two-probe system was used for the current measurement and the average value was evaluated through 20 different devices. The IV plot shows minimum, median, and maximum values among 20 devices, and is drawn with different Si roughness. As shown in the logarithm plot, almost all devices show constant current before the CR, whereas the current of the device with a larger roughness than the CR is increased. Therefore, the CR value defined by the simple method in this study proved to be effective. Although the CR value in the experiment is not an absolute criterion for all high-k insulating films, we believe that the proposed methodology will be valuable for establishing an industrial standard.

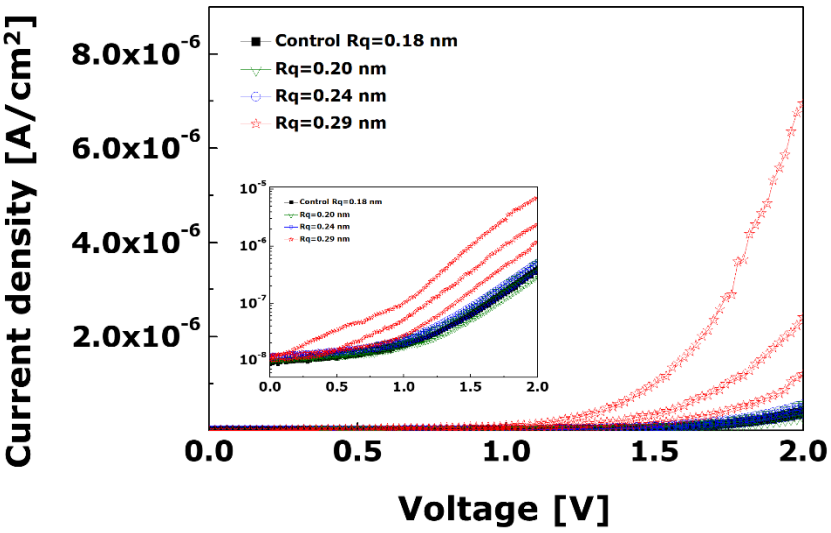

Figure 3.22 Current density plot of the minimum, median, and maximum data. (inset) A logarithm plot of the current density.

3.3.6 Inline applications for the morphology analysis of ultrathin hafnium oxide films

An ultrathin HfO_2 layer was inspected in tapping mode using a silicon tip (RTESPA-300; Bruker, USA) with a normal probe radius of 8 nm and a cantilever spring constant of 40 N/m. The cantilever was oscillated at 25 nm (free-air amplitude) and the set-point was 15 nm. During the semiconductor process, the probe is very quickly engaged on the sample with a digital signal processor control within a few seconds to ensure no damage to the probe. The temperature variation in the acoustic shielding chamber was held under 0.1℃ at room temperature. Vibration was eliminated through feedback from the special linear motor used with a granite air-floating and anti-vibration table. The AFM feedback motion was conducted by changing the amplitude of the oscillating probe with an image isolation™ function. This method isolates the background frequency and the special fingerprint frequency from the environment before the image scan.

During the inline fabrication process, surface morphology measurements of the sub-nanoscale roughness are among the most challenging applications in a typical facility environment. It requires a high performance of the anti-vibration efforts and acoustic shielding while executing atomic force feedback control on the surface. In addition, there are many items to be considered to achieve reliable data [35, 36].

Thus, we undertook a surface analysis of a mass-produced ultrathin HfO_2 film sample (~ 3 nm in thickness) using an optimized LN AFM system. Subsequently, roughness measurements of an identical mass-produced HfO_2 wafer were conducted using an inline AAFM system (InSight; Bruker Corporation, USA), including an auto-level stage, automated probe exchange, and thermal stability, the process of which is fully automated for the mass production of these wafers. A highly accurate laser interferometer stage was used for the measurements. The resonance frequency of the AAFM itself and the fingerprint frequency of the environmental noise in the semiconductor facility were separated to obtain sub-nanoscale roughness with the in-line AAFM system. The background noise level was approximately 35 pm.

The roughness parameters calculated from each topography image are summarized in Table 3.3. All roughness parameters are similar except for that in the area with a low FOV of 50 nm. A small scanning area (50 nm FOV) led to differences due to the lateral resolution limit in that case. The average value of the RMS roughness is 0.11 nm and the dynamic repeatability and reproducibility (R&R) value is below 30 pm (the 3σ value for 10 measurements). There are minor differences between the two results, as shown in Table 2. This subtle difference is considered to be caused by the different measurement environments and by the tip conditions. Thus, the results showed good consistent with the LN-AFM outcome

within the tool performance specifications.

The present study utilized roughness scaling metrology for an ultrathin dielectric layer, hafnium oxide film, as utilized in the semiconductor manufacturing process. The effect of the substrate roughness on the roughness of a 3-nm-thick hafnium oxide overlayer was investigated using low-noise AFM. The overlayer roughness (HfO2 films) is less affected by the low roughness of Si substrates, but the interface effect became severe only when the maximum peak-to-valley parameter of the initial substrate was close to the thickness of the hafnium film (underlayer Rt ~ 3 nm). Thus, the CR value can be determined from the intersection of the two linear fits. The CR values of the overlayer and the underlayer were 0.18 nm and 0.27 nm, respectively. In addition, the effectiveness of the defined CR was confirmed by measuring the leakage current of the MIM structure.

We also confirmed the effects of sub-nanometer roughness management in an actual fabrication environment by applying an inline AAFM technique developed for a mass-produced monitor. The dynamic repeatability and reproducibility (R&R) of the roughness information for the mass-produced hafnium oxide films are in good agreement with those of LN AFM. Hence, the results here will contribute to development, enhance the production yields of semiconductors, and ensure reliable standardization metrology for surface roughness levels.

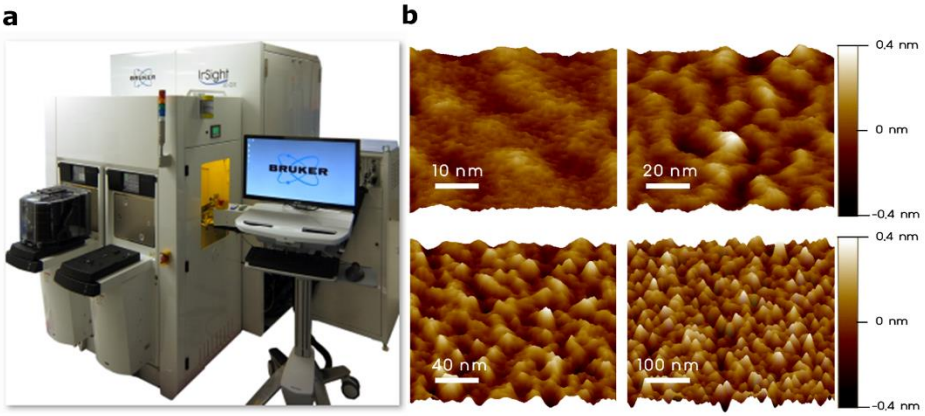

Figure 3.23 (a) Photograph of Bruker's inline production auto-AFM. (b) AFM image of a hafnium oxide thin layer demonstrating the capability of roughness measurements in a fabrication facility (Fab) environment.

Table 3.3 Roughness parameters extracted from each topography image.

	FOV [nm]	R_a [nm]	R_q [nm]	R_t [nm]
LN AFM	50	0.09	0.11	0.80
	100	0.10	0.13	0.82
	200	0.09	0.12	0.84
	500	0.09	0.12	0.98
Inline AAFM*	50	0.06	0.08	0.72
	100	0.09	0.11	0.75
	200	0.09	0.11	0.78
	500	0.08	0.10	0.83

*Note: image isolation was performed for inline AAFM data.

3.4. Reference

[1] G.D. Wilk, R.M. Wallace, J. Anthony, High-κ gate dielectrics: Current status and materials properties considerations, *Journal of applied physics*, 89, **2001**, 5243-5275.

[2] E.M. Vogel, Technology and metrology of new electronic materials and devices, in: Nanoscience And Technology: A Collection of Reviews from Nature Journals, *World Scientific*, **2010**, pp. 166-173.

[3] R.P. Ortiz, A. Facchetti, T.J. Marks, High-k organic, inorganic, and hybrid dielectrics for low-voltage organic field-effect transistors, *Chemical reviews*, 110, **2009**, 205-239.

[4] C. Shin, K. Kim, J. Kim, W. Ko, Y. Yang, S. Lee, C.S. Jun, Y.S. Kim, Fast, exact, and non-destructive diagnoses of contact failures in nano-scale semiconductor device using conductive AFM, *Scientific reports*, 3, **2013**, 2088.

[5] Y. Sugimoto, P. Pou, M. Abe, P. Jelinek, R. Pérez, S. Morita, O. Custance, Chemical identification of individual surface atoms by atomic force microscopy, *Nature*, 446, **2007**, 64.

[6] T.G. Kuznetsova, M.N. Starodubtseva, N.I. Yegorenkov, S.A. Chizhik, R.I.

Zhdanov, Atomic force microscopy probing of cell elasticity, *Micron*, 38, **2007**, 824-833.

[7] T. Bao, D. Fong, S. Hand, Automated AFM as an Industrial Process Metrology Tool for Nanoelectronic Manufacturing, in: Applied Scanning Probe Methods X, *Springer*, **2008**, pp. 359-412.

[8] R. Dixson, R.S. Goldband, N.G. Orji, Lateral tip control effects in CD-AFM metrology: the large tip limit, in: Scanning Microscopies 2015, *International Society for Optics and Photonics*, **2015**, pp. 96360Q.

[9] R. Dixson, B.P. Ng, N. Orji, Effects of lateral tip control in CD-AFM width metrology, *Measurement Science and Technology*, 25, **2014**, 094003.

[10] G. Dai, W. Häßler-Grohne, D. Hüser, H. Wolff, H.-U. Danzebrink, L. Koenders, H. Bosse, Development of a 3D-AFM for true 3D measurements of nanostructures, *Measurement science and technology*, 22, **2011**, 094009.

[11] G. Dai, W. Hässler-Grohne, D. Hueser, H. Wolff, J. Flügge, H. Bosse, New developments at Physikalisch Technische Bundesanstalt in three-dimensional atomic force microscopy with tapping and torsion atomic force microscopy mode and vector approach probing strategy, *Journal of Micro/Nanolithography, MEMS, and MOEMS*, 11, **2012**, 011004.

[12] G. Dai, K. Hahm, F. Scholze, M.-A. Henn, H. Gross, J. Fluegge, H.

Bosse, Measurements of CD and sidewall profile of EUV photomask structures using CD-AFM and tilting-AFM, *Measurement Science and Technology*, 25, **2014**, 044002.

[13] G. Dai, K. Hahm, H. Bosse, R.G. Dixson, Comparison of line width calibration using critical dimension atomic force microscopes between PTB and NIST, *Measurement Science and Technology*, 28, **2017**, 065010.

[14] G. Dai, F. Zhu, M. Heidelmann, G. Fritz, T. Bayer, S. Kalt, J. Fluegge, Development and characterisation of a new line width reference material, *Measurement Science and Technology*, 26, **2015**, 115006.

[15] A. Määttänen, P. Ihalainen, B. Törngren, E. Rosqvist, M. Pesonen, J. Peltonen, Hierarchically structured self-supported latex films for flexible and semi-transparent electronics, *Applied Surface Science*, 364, **2016**, 37-44.

[16] J. Park, C. Shin, M. Kim, J. Kim, J. Park, J. Kim, C. Jun, Y. Yim, J. Lee, Exact and reliable overlay metrology in nanoscale semiconductor devices using an image processing method, in, *SPIE*, **2014**, pp. 7.

[17] G. Borionetti, A. Bazzali, R. Orizio, Atomic force microscopy: a powerful tool for surface defect and morphology inspection in semiconductor industry, *The European Physical Journal-Applied Physics*, 27, **2004**, 101-106.

[18] J. Gong, D.J. Lipomi, J. Deng, Z. Nie, X. Chen, N.X. Randall, R. Nair,

G.M. Whitesides, Micro-and nanopatterning of inorganic and polymeric substrates by indentation lithography, *Nano letters*, 10, **2010**, 2702-2708.

[19] Y.F. Dufrêne, T. Ando, R. Garcia, D. Alsteens, D. Martinez-Martin, A. Engel, C. Gerber, D.J. Müller, Imaging modes of atomic force microscopy for application in molecular and cell biology, *Nature nanotechnology*, 12, **2017**, 295.

[20] M.S. Diware, H.M. Cho, W. Chegal, Y.J. Cho, S.W. O, S.-H. Paek, D.S. Kim, K.-S. Kim, Y.G. Min, J.H. Jo, Label-free detection of hepatitis B virus using solution immersed silicon sensors, *Biointerphases*, 12, **2017**, 01A402.

[21] G. Eda, G. Fanchini, M. Chhowalla, Large-area ultrathin films of reduced graphene oxide as a transparent and flexible electronic material, *Nature nanotechnology*, 3, **2008**, 270.

[22] K.-H. Lim, J.-E. Huh, J. Lee, N.-K. Cho, J.-w. Park, B.-i. Nam, E. Lee, Y.S. Kim, Strong Influence of Humidity on Low-Temperature Thin-Film Fabrication via Metal Aqua Complex for High Performance Oxide Semiconductor Thin-Film Transistors, *ACS applied materials & interfaces*, 9, **2016**, 548-557.

[23] H. Kwon, S.W. Seo, T.G. Kim, E.S. Lee, P.T. Lanh, S. Yang, S. Ryu, J.W. Kim, Ultrathin and flat layer black phosphorus fabricated by reactive oxygen

and water rinse, *ACS nano*, 10, **2016**, 8723-8731.

[24] J.C. Hackley, T. Gougousi, J.D. Demaree, Nucleation of HfO2 atomic layer deposition films on chemical oxide and H-terminated Si, *J. Appl. Phys.*, 102, **2007**, 034101.

[25] E.P. Gusev, C. Cabral, M. Copel, C. D'Emic, M. Gribelyuk, Ultrathin HfO2 films grown on silicon by atomic layer deposition for advanced gate dielectrics applications, *Microelectron. Eng.*, 69, **2003**, 145-151.

[26] S. Watanabe, N. Nakayama, T. Ito, Homogeneous hydrogen-terminated Si(111) surface formed using aqueous HF solution and water, *Appl. Phys. Lett.*, 59, **1991**, 1458-1460.

[27] P. Dumas, Y.J. Chabal, P. Jakob, Morphology of hydrogen-terminated Si(111) and Si(100) surfaces upon etching in HF and buffered-HF solutions, *Surf. Sci.*, 269-270, **1992**, 867-878.

[28] K. Kolanek, M. Tallarida, M. Michling, D. Schmeisser, In situ study of the atomic layer deposition of HfO2 on Si, *J. Vac. Sci. Technol.*, 30, **2012**, 01A143.

[29] K. Kolanek, M. Tallarida, D. Schmeisser, Height distribution of atomic force microscopy images as a tool for atomic layer deposition characterization, *J. Vac. Sci. Technol.*, 31, **2013**, 01A104.

[30] W. Lau, J. Zhang, X. Wan, J. Luo, Y. Xu, H. Wong, Surface smoothing effect of an amorphous thin film deposited by atomic layer deposition on a surface with nano-sized roughness, *AIP Advances*, 4, **2014**, 027120.

[31] M. Ritala, M. Leskelä, J.P. Dekker, C. Mutsaers, P.J. Soininen, J. Skarp, Perfectly conformal TiN and Al2O3 films deposited by atomic layer deposition, *Chem. Vap. Deposition*, 5, **1999**, 7-9.

[32] Y. Wang, M.T. Ho, L.V. Goncharova, L.S. Wielunski, S. Rivillon-Amy, Y.J. Chabal, T. Gustafsson, N. Moumen, M. Boleslawski, Characterization of Ultra-Thin Hafnium Oxide Films Grown on Silicon by Atomic Layer Deposition Using Tetrakis(ethylmethyl-amino) Hafnium and Water Precursors, *Chem. Mater.*, 19, **2007**, 3127-3138.

[33] G.G. Ting, O. Acton, H. Ma, J.W. Ka, A.K.-Y. Jen, Study on the Formation of Self-Assembled Monolayers on Sol− Gel Processed Hafnium Oxide as Dielectric Layers, *Langmuir*, 25, **2009**, 2140-2147.

[34] J. Lee, K. Yoon, K.-H. Lim, J.-W. Park, D. Lee, N.-K. Cho, Y.S. Kim, Vertical Transport Control of Electrical Charge Carriers in Insulator/Oxide Semiconductor Hetero-structure, *Sci. Rep.*, 8, **2018**, 5643.

[35] S.-w.W. Chen, J.-L. Pellequer, DeStripe: frequency-based algorithm for removing stripe noises from AFM images, *BMC Struct. Biol.*, 11, **2011**, 7.

[36] P. Fechner, T. Boudier, S. Mangenot, S. Jaroslawski, J.N. Sturgis, S. Scheuring, Structural Information, Resolution, and Noise in High-Resolution Atomic Force Microscopy Topographs, *Biophys. J.*, 96, **2009**, 3822-3831.

Chapter 4 Applications of indentation lithography

4.1 Patterned organic films for 3D depth profiles of TOF-SIMS imaging

4.1.1 Fabrication method of organic dual layer for 3D TOF-SIMS

Prior to the fabrication of the indentation patterns, micropatterns were produced by photolithography as shown in Fig. 4.1 below. While increasing the line width, various sizes were produced, and the minimum line width was 1 μm. SU-8 or GXR 601 photoresist (PR) was used as the organic layer. After the formation of the PR patterns, the substrate was subjected to O_2 plasma treatment. Trehalose was then spin-coated at 2000 RPM and applied onto the patterned PR layer.

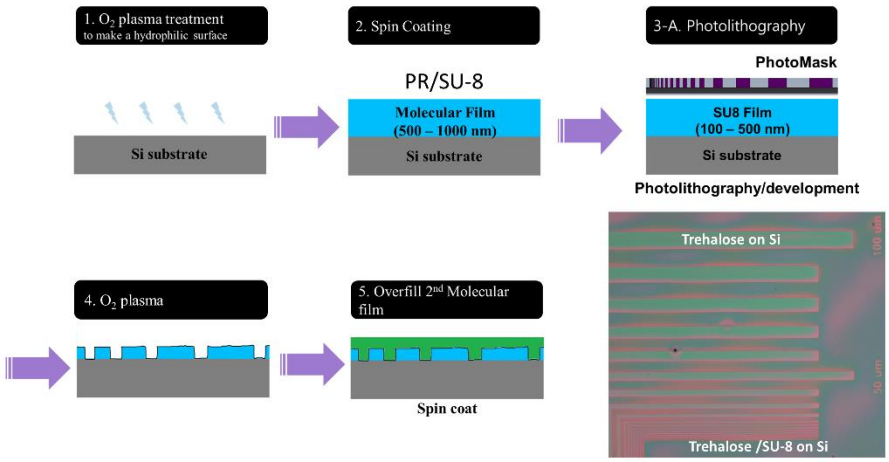

Figure 4.24 Fabrication flow of organic dual layer using photolithography

4.1.2 Results for organic dual layer for 3D TOF-SIMS

Image analysis was performed through TOF-SIMS [1]. The result was different from the expectation. The PR layer was penetrated below the substrate. That is, image distortion occurs in the depth direction. The reason for the interruption was thought as the two materials have different etch rate during the sputtering with argon clusters [2, 3]. Therefore, for the real bio-imaging, a three-dimensional patterned bio-standard sample is required.

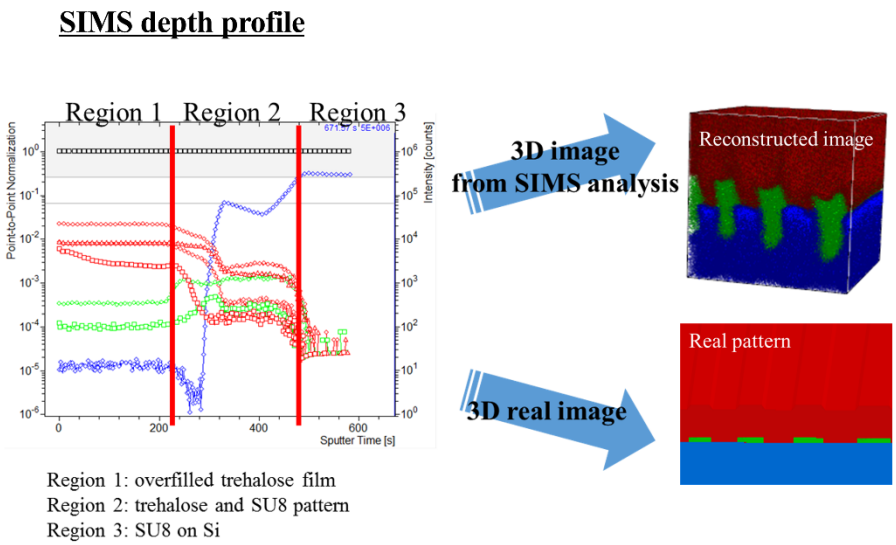

Figure 4.25 Depth profile of organic layer

4.1.3 Fabrication issues of patterned organic dual layer

In order to produce patterned bi-layer of the actual bio-specimens, a number of fabrication issues must be solved.

- Bio materials are random structures: too many uncertainties in structure and chemistry. So chemically known composition required
- No intermixing molecules between two organic-materials (i.e. A: trehalose, B: cholesterol)
- Surface property of cholesterol (hydrophobic) and trehalose (hydrophilic). Spin casting is not allowed.
- No waviness surface is required: it causes the image distortion for depth profiling.
- The top layer of the reference sample should be thin. (few micron or nanometer scale)
- Method to make micro/nano patterns required.

To address these issues, we chose two substances, trehalose and cholesterol. Although the cholesterol is an amphipathic substance, it exhibits hydrophobic properties when deposited on a substrate and has the advantage of no-intermixing with the trehalose. Thus, the cholesterol was deposited via the physical vapor

deposition (PVD) method following the literature [4-6]. The deposition was carried out at 10^{-5} Torr through a vacuum chamber. During the deposition process, the substrate was cooled through liquid nitrogen, and the temperature was transferred through the cold finger contact. The deposition was carried out for an hour and the thickness of the produced cholesterol was about 500 nm.

After the cholesterol film was deposited, the indentation process was performed as shown in Fig. 4.5. The LN-AFM was used for the nano-patterns, and the stylus force of the alpha step was controlled for the micro-patterns. When the cholesterol layer was patterned, a trehalose layer was formed by drop casting. Prior to covering the top layer, the line width of the pattern was measured by AFM equipment. The line width of the currently fabricated sample was about 5 μm.

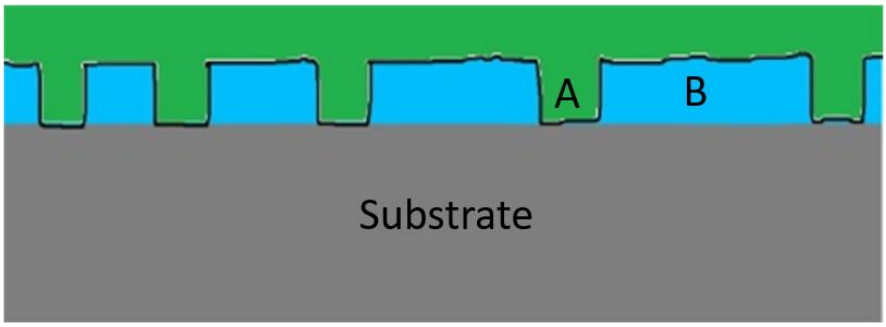

Figure 4.26 Cartoon for patterned organic-dual layer. The figure shows the goal for this project.

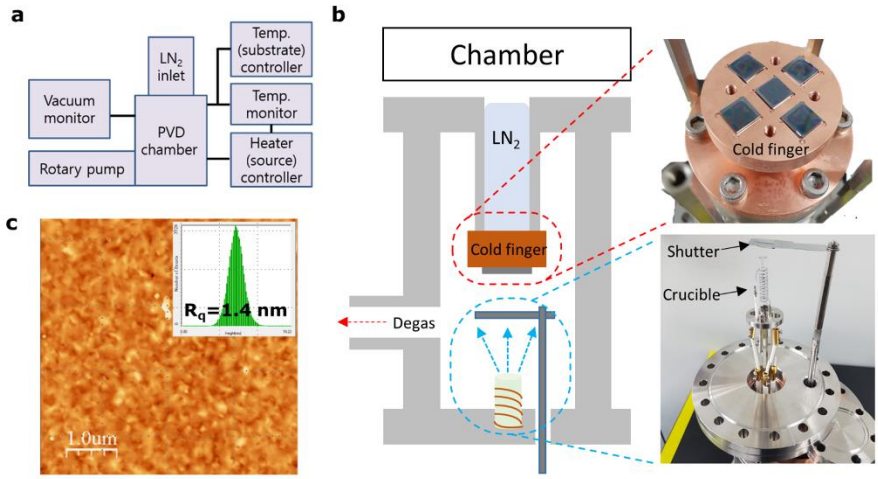

Figure 4.27 (a) PVD setup for cholesterol film. (b) schematic image and photographs of PVD chamber. (c) Surface of the cholesterol film taken by low-noise AFM. RMS roughness = 1.4 nm.

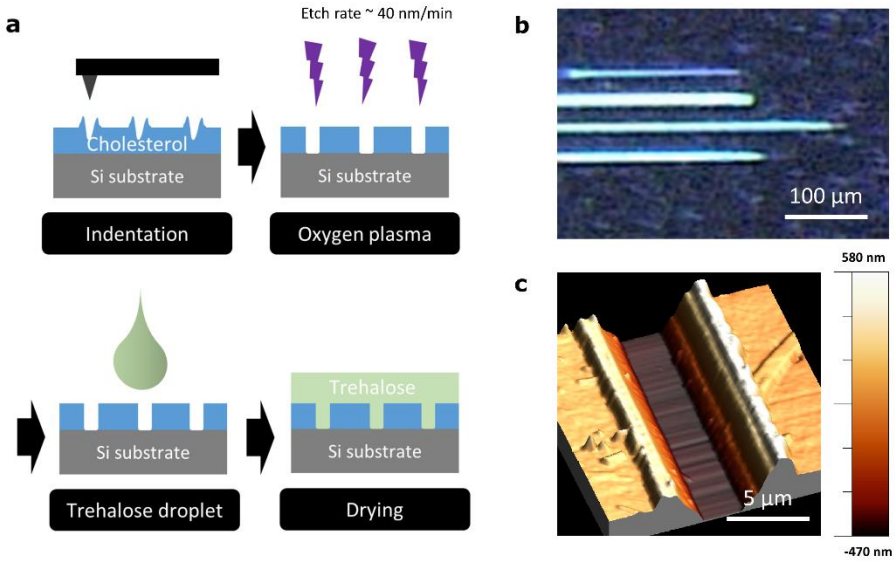

Figure 4.28 (a) schematic illustrations for fabrication processes. (b) Optical microscope image of the patterned cholesterol film. (c) AFM image of patterned cholesterol film before overfilling the Trehalose.

4.1.4 3D depth profile of patterned organic dual layer

ToF-SIMS experiments were performed by using an IONTOF TOF. SIMS 5 (ION-TOF GmbH, Münster, Germany) was equipped with two ion sources. A liquid metal ion gun (LMIG) was used to generate a pulsed 30 keV Bi3+ beam, whereas an electron impact gun was used to generate a 5 keV Ar1500+ beam. Both beams hit the target at an angle of 45°. A positive ion spectra were internally calibrated using total ion intensity normalized to the respective secondary total ion yields.

For the 3D data sets, the Bi3+ beam was rastered over a 200 μm × 200 μm (varies between data sets) and centered inside a 600 μm × 600 μm Ar1500+ crater. In order to obtain the 3D imaging experiments, the mass resolution (m/Δm) at m/z=50 was roughly 300 for the imaging modes. Target currents were measured before each data set with use of a Faraday cup.

The 30 keV Bi3+ current was typically 0.04−0.05 pA with an 80.1 ns pulse width for the imaging mode, while the 5 keV Ar1500+ current varied between data sets. The Ar1500+ puttering time was set to 2 sec, to achieve a constant sputter dose of 1.25 × 1012 ions/cm2 for each sputter cycle. Analysis cycles with a Bi3+ sputter dose of 5.8 × 1011 ions/cm 2 were used to acquire images (256 × 256 pixels) at each slice.

The first TOF-SIMS image of 3D patterned organic-dual layer was obtained. Unfortunately, the image distortion was still happening. The trehalose molecules were penetrated into the Si. Therefore, calibration process is required for the 3D depth profiling of organic films.

It is necessary to perform a number of experiments in the future to examine why this image distortion occurs. It also is required to determine whether the image distortion is caused by the beam direction, and the beam intensity to be adjusted. It is also important to understand the degree of image distortion by changing the materials that fill the patterns. Creatinine (density, ρ = 1.09 g/cm^3) and fructose (ρ = 1.69 g/cm^3) are candidates. The dependence of primary ion beam on the cholesterol (ρ = 1.05 g/cm^3)/creatinine film if the densities of the materials are similar.

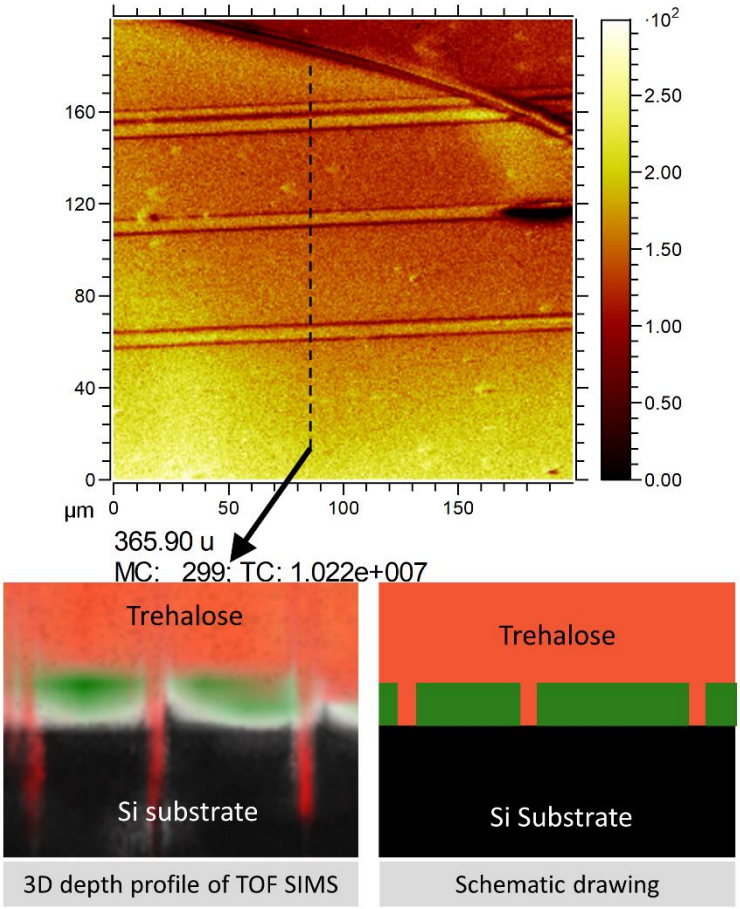

Figure 4.29 The results of 3D TOF-SIMS imaging for the patterned organic dual layer. The green layer represents the cholesterol film.

4.2 Bulge-free indentation technique

4.2.1 PMMA bulge removal using IPA/DI developer

A poly(methyl metacrylate) (PMMA) layer exposed to the electron beam selectively can be effectively desolved in IPA/water bi-solvent developer. The electron beam breaks the long chain of PMMA and eventually produces low molecular weight polymers, which is selectively decomposed by the developer [7, 8]. Interestingly, mechanically damaged PMMA (not exposed by electron beam nor illuminated by UV lights) can be also effectively elliminated by the IPA/water developer. This phenomenon is independent of the size of the bulge. In other words, both of the micro-bulges generated by the scratch process and the nano-bulge generated during the nanoindentation process are selectively removed from the IPA / water developer.

For the indentation process, custom-designed software was used to define and fabricate the lithographic surface patterns. In the initial stage, the target images such as holes, lines, or pictures were recorded. The AFM probe was moved to a predefined position, where the scanner was stepped up to the predefined extension (Δz) in the z direction with the feedback loop turned off. Then, the designed patterns were pressed into a resist layer which is pre-deposited on the sample surface. Since

contact mode operation frequently damaged the PMMA surface due to the large spring constant of the probe used, the AFM was operated in a tapping mode for indenting the PMMA layer.

PMMA (950,000 molecular weight, 2% dissolved in anisole from MicroChem Corp., USA) of ~ 100 nm thickness was spin-coated on a glass or Au-coated SiO2/Si substrate, which was cleaned in an ultrasonic bath of acetone prior to the coating process. The pinhole-free PMMA film was then baked at 170℃ in an oven. Nanoindentation patterns on the PMMA layer were made using 7 nm diameter, conical, single crystal diamond probes (SCD, MikroMasch, USA) in a commercial AFM unit (SPA-400, Seiko Instruments, Japan). Also, in order to investigate on the dependency of IPA/DI water mixing ratios, we fixed other conditions such as humidity and process time. Dented holes were inspected in tapping mode AFM using ultrasharp high density carbon tips (HDC, Nanotools, Germany) having a nominal probe radius of 2 nm.

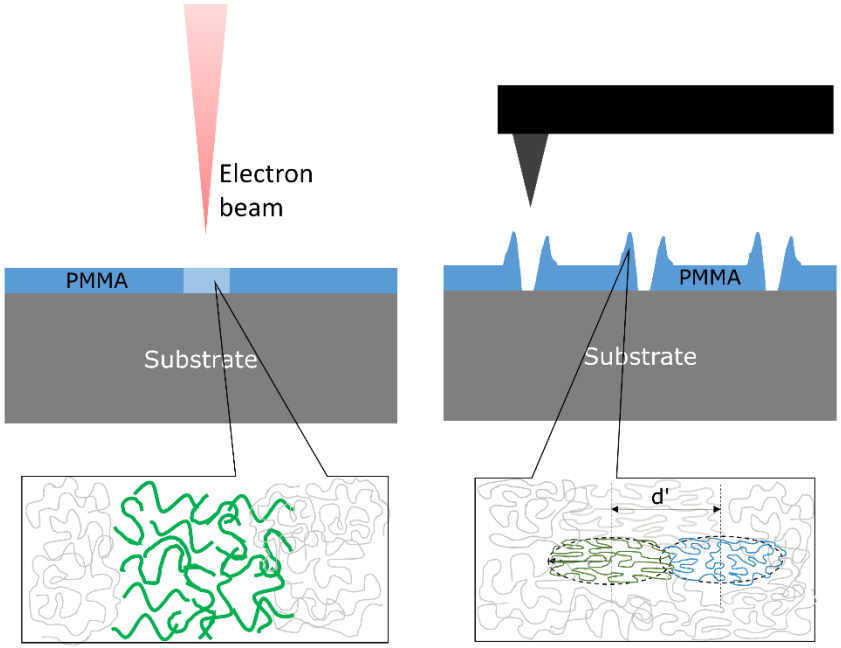

Figure 4.30 Deformation of PMMA during electron beam lithography and indentation lithography.

Fig. 4.8a shows the process of the bulge-free indentation lithography. When the PMMA was penetrated by the AFM tip, the bulges were formed around the tip. The bulge-free nano dot array can be produced after immersing the patterened sample in a developer for 10 minutes. Two typical line scans exhibit that the protrusions have been selectively removed. Integrations of the bulge heights and the hole depths were performed to confirm the residual bulge heights and the size of the patterns. The baseline was taken as zero, which represents the pristine PMMA surface. As a result of integrating the heights of the bulges and the depths of the holes, it was confirmed that the bulge was clearly removed.

Soft matters are likely to recover through the self-healing process [9, 10]. However, the bulge produced by the indentation was not healed when immersed in the developer. The bulges were dissolved by the developer. This can be deduced from the fact that the volume was about two-fold increased since the development as shown in Fig. 4.8e. These selective bulge removal phenomena and mechanisms will be discussed further in the following sections.

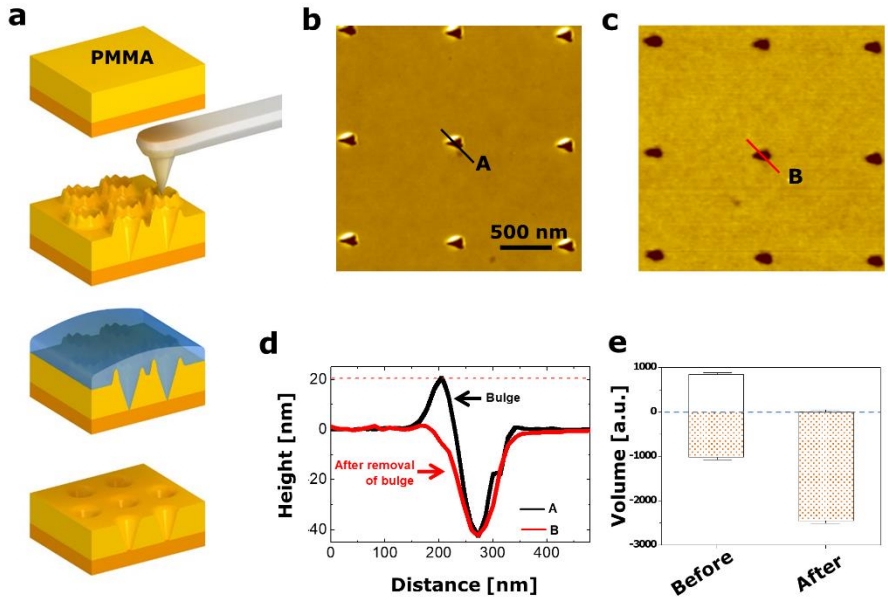

Figure 4.31 (a) Schematic process of Bulge-free indentation lithography. (b) AFM surface image of generated bulges. (c) Bulge removal using developer. (d) Line profiles before and after the immersing in the developer. (e) Volume changes of indented pattern. The positive and negative volumes represent the bulge and the dent pattern, respectively.

4.2.2 Mechanism study on the selective bulge removal process

The observed dissolution of the damaged PMMA in the mixture of IPA and DI water (5:1) is known as a cosolvency that a polymer chain can swell in a mixture of two miscible poor solvents, while the identical polymer collapses in these two individual components [7, 11-14]. The adoption of water to pure IPA effectively induces hydration shell around the individual PMMA molecules by the formation of hydrogen bonding to the ester group of PMMA. This phenomenon enhances the solubility of PMMA until the increased polarity of the solvent mixture leads to the formation of water clusters as the amounts of water increase. More recently, Mukherji et. al. reported that the subtle balance of entropically driven depletion interactions between polymer and cosolvents promotes polymer swelling in poor solvent mixtures [15]. However, the central question in understanding this bulge-free nanopattern is, how the bulge formed around the pattern is preferentially removed by the simple cosolvent treatment. New insight into the selective removal of polymer in the pile-up regions upon indentation comes from the recent theoretical and experimental studies that suggest the dynamics of polymer chain as well as their deformation are accelerated when the Gaussian chain conformation of polymer melts is perturbed under confinement in thin films.

Indentation of a smooth polymer film produces a patterned surface, inevitably

accompanied by the large-strain deformation along with viscous flow of a polymer melt. Average height and width of bulges are about ~20 and 100 nm, respectively. These length scales are comparable to the unperturbed size (i.e. radius of gyration, R_g ~ 33 nm) of the polymer molecule. During the process, the chain conformation in the pile-up region should be modified by the large-scale rheological response (i.e. squeeze flow) of topologically entangled polymer melts to an applied load, which imposes a severe confinement as well as both tensile and compressive stress. In particular, these squeezed polymer molecules with the inelastic strain at similar length scale to the R_g can induce local entanglement depletion, which leads to the reduced relaxation time of entangled polymer melts. Moreover, the suppression of intermolecular entanglement effectively weakens the transient interpenetrating polymer network, preferentially swollen by the solvent mixture and eventually washed out. As a result, the transport process (i.e. dissolution) of polymer molecules, perturbed by squeeze flow in the pile-up, into a solvent is significantly accelerated compared to the unperturbed counterpart, and thus, the bulge can be selectively removed.

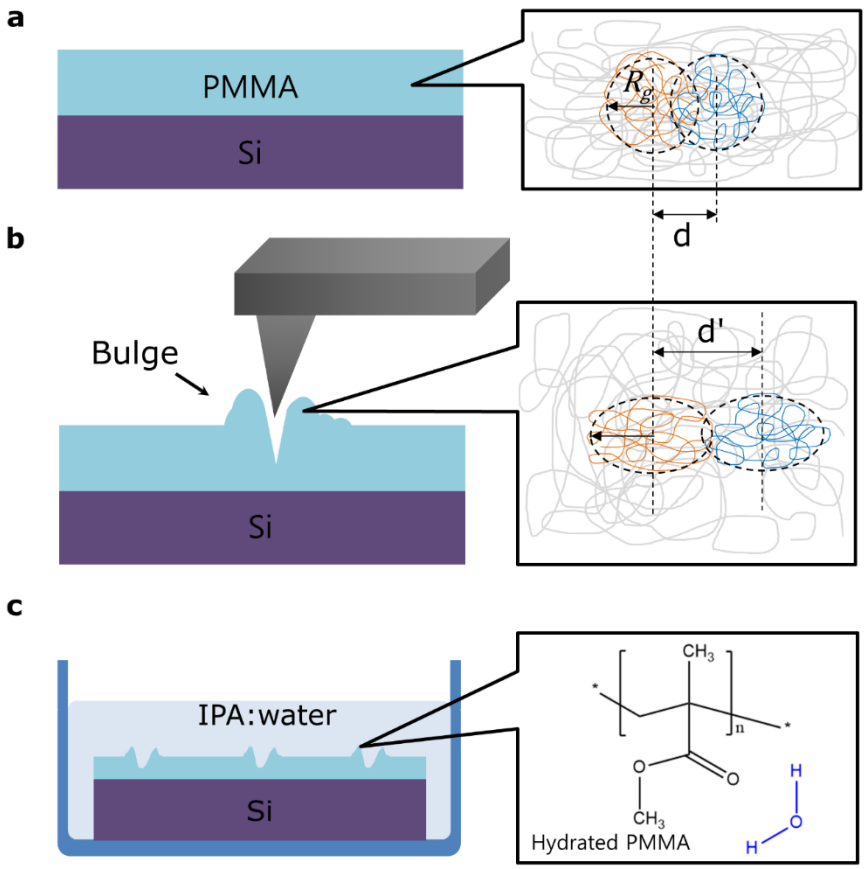

Figure 4.32 Schmetic illustration of the dis-entanglement of PMMA during dent process. (a) Entanglement of PMMA by spin casting process. The thickness of the PMMA is about 100 nm in the experiments. (b) The deformation of the PMMA by indentation process. The inset figure shows the local entanglement depletion so the distance between two neighbor chains was increased (d < d‘). (c) The hydrated PMMA in the IPA/water developer is dependent upon the degree of the interpenetration between neighbor chains.

4.2.3 Optimal condition for bulge-free indentation

As discussed above, the indentation patterns can be controlled by the concentration of the developer and the molecular weight of the PMMA. The concentration of the developer will contribute to the melting of the hydrated PMMA, and the degree of the entanglement with different R_g values will be related to the selectivity of the bulge and pristine PMMA. Thus, optimization of pattering process is required depending on the different R_g values and the radii of gyration can be estimated by Flory-Fox equation:

$$R_g = \mathrm{a}\sqrt{\frac{M_w/M_0}{6}}, \qquad (4.4)$$

where a is the monomer segment length (0.65 nm) and M_0 is the molar mass of the PMMA monomer ($100.12\ g \cdot mol^{-1}$) [16, 17]. Thus, the radii of gyration of 23k, 77k, 120k, 950k, and 2903k PMMA, which were used in the experiments, were determined to be 4, 7.4, 9.2, 25.8, and 45 nm, respectively.

The results for the optimization process by varying the M_w of PMMA are shown in the Fig. 4.10 and 4.11. The etch rate represents the changes in PMMA thickness by the developer. The sum of bulge height is denoted by B and the ΔB is

the changes in the bulge height after dissolution in the developer. Conclusively, the larger the difference between etch rate and ΔB/B values shown in the results of Fig. 4.11, the more optimized the patterning condition.

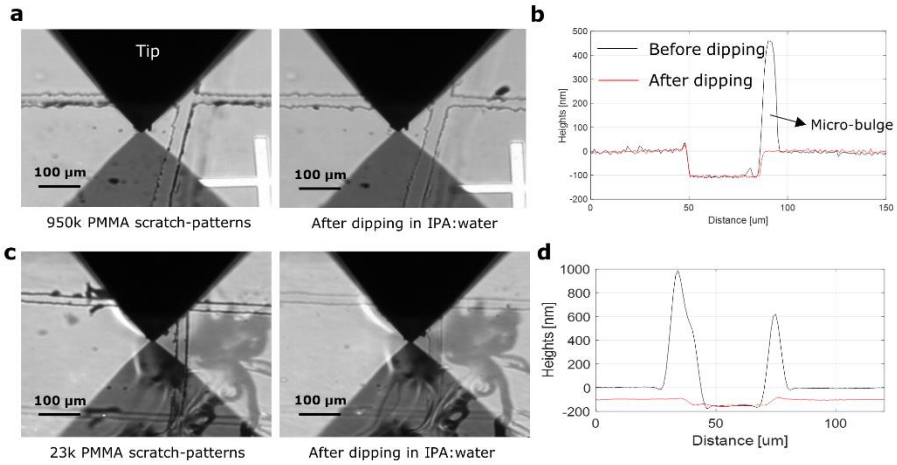

Figure 4.33 (a) Optical microscope images of scratch patterns on 100 nm thick PMMA (Mw = 950 kDa) layer. Before (left) and after (right) dipping in the developer. (b) A plot of line scans before and after dipping in the developer. (c) Optical microscope images of scratch patterns on 100 nm thick PMMA (Mw = 23 kDa) layer. (d) Line profiles of the 23 k PMMA film.

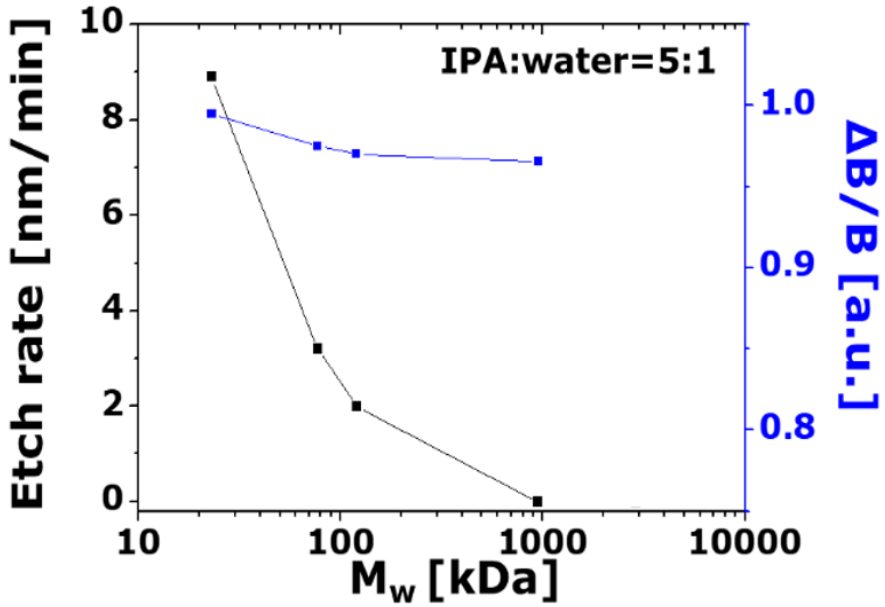

Figure 4.34 The changed thickness of the PMMA films by the IPA/water (5:1) developer depending on the average molecular weight (left). The changes in bulge height by the developer (right).

4.2.4 3D bulge-free nano-patterns

The removal process of bulges from the PMMA can be useful in fabricating various multi-tiered master patterns. Soft lithography is receiving much attention because it can be easily applied to the advanced devices as well as biological applications such as the platform of lab-on-a-chip [18-21]. In soft lithography, the manufacture of a master pattern is a prerequisite. E-beam lithography is widely used to manufacture master nanopatterns, but this approach is expensive and necessary to meet severe conditions such as charging issue of the substrates, dose-test for appropriate beam exposing, and inspections using other equipment. Moreover, in conventional lithography, it is still challenging to manufacture three-dimensional master nanopatterns for multi-tiered nanostructures. The indentation lithography has been considered as a good alternative for fabricating multi-tiered nanostructures, however, the bulges have blocked the exact formation of size, shape and multi-tiered structure with a nanometer scale, so far. Therefore, the bulge-free process in this study will give the key to resolve the critical problems of indentation lithography.

Various multi-tiered nanostructures were fabricated using raster and vector scan methods. Subsequently, bulge-free patterns were obtained by adopting IPA/water developer. In the bulge-free method after indentation lithography, we produced not

only simple dent holes, but also line and complex images with multi-tiered structures for nanoscale mold. During the repeated indentation lithography, a diamond probe was used to minimize the deformation of the indentation patterns and the complex multi-tiered structures were successfully fabricated. The dent holes of different sizes can be fabricated by changing the probe loading force and the bulges of the PMMA were removed altogether. Furthermore, we fabricated the bulge free continuous nanopatterns with different depths, such as flower-pattern inside a nanometer scaled cup. Comparing with the isolated multi-tiered nanostructure, these continuous multi-tiered nanopetterns suggest that it is possible to increase dramatically the density in the structure and fabricate the sophisticated shapes with nanometer scale.

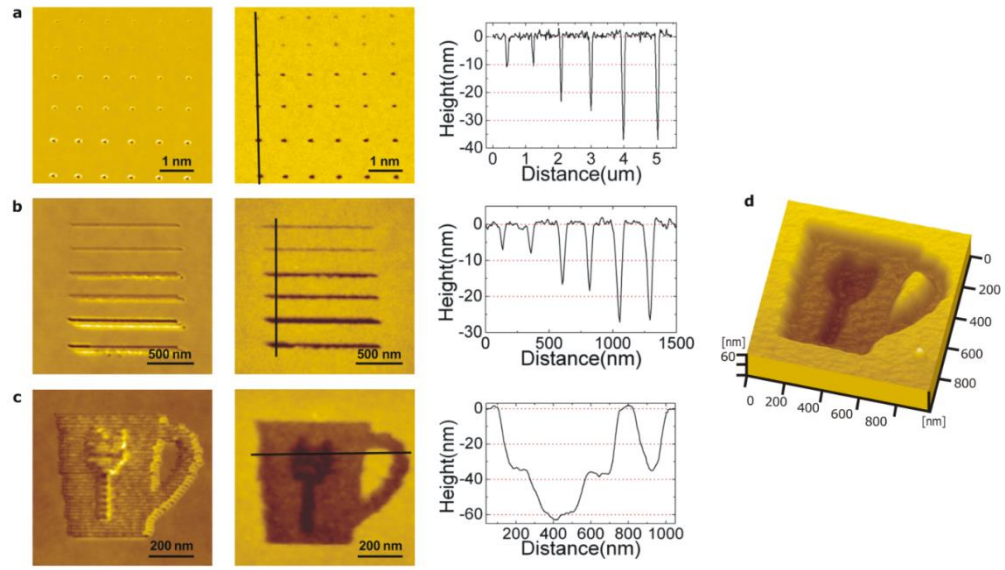

Figure 4.35 (a) Dot pattern images and line profile with different depths of 10, 22, and 38 nm. (b) Line pattern image and line profile with different depths of 8, 18 and 28nm (c) Image of an indentation pattern of a cup and with a flower. Depth of the cup pattern is about 35nm and flower pattern is about 60nm as shown in the cross-sectional line profile. (d) An expanded three-dimensional image of multi-tiered pattern and showing the nano-flower pattern with the different depth in cup pattern.

4.3. Reference

[1] P.D. Piehowski, A.J. Carado, M.E. Kurczy, S.G. Ostrowski, M.L. Heien, N. Winograd, A.G. Ewing, MS/MS methodology to improve subcellular mapping of cholesterol using TOF-SIMS, *Analytical chemistry*, 80, **2008**, 8662-8667.

[2] A.J. Barlow, J.F. Portoles, P.J. Cumpson, Observed damage during Argon gas cluster depth profiles of compound semiconductors, *Journal of Applied Physics*, 116, **2014**, 054908.

[3] A.S. Mohammadi, N.T. Phan, J.S. Fletcher, A.G. Ewing, Intact lipid imaging of mouse brain samples: MALDI, nanoparticle-laser desorption ionization, and 40 keV argon cluster secondary ion mass spectrometry, *Analytical and bioanalytical chemistry*, 408, **2016**, 6857-6868.

[4] D. Willingham, A. Kucher, N. Winograd, Molecular depth profiling and imaging using cluster ion beams with femtosecond laser postionization, *Applied Surface Science*, 255, **2008**, 831-833.

[5] K. Shen, D. Mao, B.J. Garrison, A. Wucher, N. Winograd, Depth profiling of metal overlayers on organic substrates with cluster SIMS, *Analytical chemistry*, 85, **2013**, 10565-10572.

[6] P.D. Piehowski, M.E. Kurczy, D. Willingham, S. Parry, M.L. Heien, N. Winograd, A.G. Ewing, Freeze-etching and vapor matrix deposition for ToF-SIMS imaging of single cells, *Langmuir*, 24, **2008**, 7906-7911.

[7] S. Yasin, D. Hasko, H. Ahmed, Comparison of MIBK/IPA and water/IPA as PMMA developers for electron beam nanolithography, *Microelectronic engineering*, 61, **2002**, 745-753.

[8] C. Vieu, F. Carcenac, A. Pepin, Y. Chen, M. Mejias, A. Lebib, L. Manin-Ferlazzo, L. Couraud, H. Launois, Electron beam lithography: resolution limits and applications, *Applied surface science*, 164, **2000**, 111-117.

[9] S. Bode, L. Zedler, F.H. Schacher, B. Dietzek, M. Schmitt, J. Popp, M.D. Hager, U.S. Schubert, Self-healing polymer coatings based on crosslinked metallosupramolecular copolymers, *Advanced Materials*, 25, **2013**, 1634-1638.

[10] R.P. Wool, Self-healing materials: a review, *Soft Matter*, 4, **2008**, 400-418.

[11] I. Fernández-Piérola, A. Horta, Cosolvents of PMMA, *Die Makromolekulare Chemie: Macromolecular Chemistry and Physics*, 182, **1981**, 1705-1714.

[12] R. Hoogenboom, C.R. Becer, C. Guerrero-Sanchez, S. Hoeppener, U.S.

Schubert, Solubility and thermoresponsiveness of PMMA in alcohol-water solvent mixtures, *Australian journal of chemistry*, 63, **2010**, 1173-1178.

[13] Y. Yu, B.D. Kieviet, E. Kutnyanszky, G.J. Vancso, S. de Beer, Cosolvency-induced switching of the adhesion between poly (methyl methacrylate) brushes, *ACS macro letters*, 4, **2014**, 75-79.

[14] B.A. Miller-Chou, J.L. Koenig, A review of polymer dissolution, *Progress in Polymer Science*, 28, **2003**, 1223-1270.

[15] D. Mukherji, C.M. Marques, T. Stuehn, K. Kremer, Depleted depletion drives polymer swelling in poor solvent mixtures, *Nature Communications*, 8, **2017**, 1374.

[16] R.L. Jones, S.K. Kumar, D.L. Ho, R.M. Briber, T.P. Russell, Chain conformation in ultrathin polymer films, *Nature*, 400, **1999**, 146.

[17] C.-C. Lin, S. Gam, J.S. Meth, N. Clarke, K.I. Winey, R.J. Composto, Do attractive polymer–nanoparticle interactions retard polymer diffusion in nanocomposites?, *Macromolecules*, 46, **2013**, 4502-4509.

[18] Y. Xia, G.M. Whitesides, Soft lithography, *Angewandte Chemie International Edition*, 37, **1998**, 550-575.

[19] G.M. Whitesides, E. Ostuni, S. Takayama, X. Jiang, D.E. Ingber, Soft lithography in biology and biochemistry, *Annual review of biomedical*

engineering, 3, **2001**, 335-373.

[20] R.S. Kane, S. Takayama, E. Ostuni, D.E. Ingber, G.M. Whitesides, Patterning proteins and cells using soft lithography, in: The Biomaterials: Silver Jubilee Compendium, *Elsevier*, **2006**, pp. 161-174.

[21] M.A. Unger, H.-P. Chou, T. Thorsen, A. Scherer, S.R. Quake, Monolithic microfabricated valves and pumps by multilayer soft lithography, *Science*, 288, **2000**, 113-116.

Chapter 5 Conclusion

5.1 Discussion and conclusion

As the semiconductor and biotechnology industries have become more developed, techniques are required to characterize the nanoscopic properties of semiconductors and biomolecular films. Many researchers have studied the surface properties of various films using SPM method [1-5].

KRISS constructed a LN-AFM system (RMS noise ~35 pm) optimized for surface metrology in the semiconductor industry and the uncertainty was estimated by a quantitative method. Furthermore, the independent external stage for low noise atomic force microscope has been developed for mid-range movements so that it aids in various measurements such as critical dimensions, roughness study, and indentation lithography. The maximum travel length of the external four-axes stage is 10 mm. For image scanning of the specific target region, the sample needs to be moved through two steps: coarse positioning with the external stage and fine positioning with PI XY piezo scanner. Prior to the CD measurements, it was confirmed that the position errors caused by the external stage and tip stage were negligible through the reproducibility experiments. In this study, custom-designed software stored the initial position of the probe and then moved it precisely to the

sample location to be measured. Subsequently, the sidewalls of an improved vertical parallel structure were measured and the repeatability and reproducibility of the CD measurements were estimated using a CDR30-EBD tip. Finally, it was proved that the external stage was working well by measuring TGX1 samples with undercut structures.

In the current semiconductor manufacturing process, the thickness parameter of ultrathin films is strictly managed on a test element group (TEG) between the chips by using spectroscopic ellipsometry. However, the thickness metrology of ultrathin films on a TEG does not reflect the actual characteristics of cell patterns; thus, on-cell metrology is required to provide more reliable surface information [6]. As the thickness of the dielectric layers becomes thinner, the task of providing the criteria pertaining to the critical roughness has attracted considerable attention, particularly in relation to surface roughness variations on devices designed with dimensions of a few nanometers. An example of this is the side wall roughness for three-dimensional nanostructures [7], such as a FinFET device. Moreover, the metrology on the side wall roughness and the effect of the underlayer on the surface wall after depositing a very thin layer remain challenging issues.

Hence, an easy, accurate, and nondestructive diagnosis of the effect on the underlayer roughness for industrial standard metrology regarding surface roughness

was reported. The surface roughness levels of HfO_2 thin films were analyzed by the LN-AFM system. The surfaces of the substrates were artificially modified using a wet chemical etching process to examine how the underlayer roughness affects the overlayer roughness, and the relationship between each fabrication step was investigated. The CR criterion of the HfO_2 thin film can be established according to the intersection between two linear fits. Simple diode devices were fabricated to verify the effectiveness of the defined CR. As a result, it was confirmed that the CR was meaningful because the amount of current increased after the CR. Subsequently, for the inline diagnosis of semiconductor fabrication, the roughness of a mass-produced hafnium oxide film was investigated. We assessed the roughness of the mass-produced HfO_2 wafer by using in-line AAFM and LN-AFM. From the results, we confirmed that the roughness of the mass-produced HfO_2 wafer with a thickness of 3 nm is below the CR value.

Time-of-Flight Secondary ion mass spectrometry (TOF-SIMS) has been a useful powerful tool for chemical imaging and depth analysis. Especially, Arn+ gas cluster ion beams in TOF-SIMS analysis have widely used not only as a primarily source for surface analysis but also as an erosion source which has a low damage cross section and a fast erosion rate for molecular depth profiling experiments. However, in order to understand an erosion mechanism for 3D depth profile in SIMS

analysis, it is necessary to calibrate with a well-defined 3D organic micro-patterns.

Here, maskless lithography (indentation) technique was employed to fabricate well-defined three dimensional organic micro-structures and TOF-SIMS was used to characterize the micro-patterns. Cholesterol film was deposited by the PVD method to produce a hydrophobic biomolecular thin film. Maskless indentation technique was used to fabricate micro-patterns on the cholesterol film. Then, Trehalose film was covered on the organic micro- structures by drop casting method. The erosion processes for GCIB on organic micro-patterns was analyzed by Bi3+ cluster ion source for TOF-SIMS will be investigated. Furthermore, we hope that it will be used as a certified standard bio-sample for 3D chemical imaging of TOF-SIMS.

At last, a simple removal method of bulges was introduced here. The PMMA layer, which was mechanically damaged, was spontaneously dissolved by the cosolvent. The optimized bulge-free indentation patterning is dependent upon the ratio of the miscible solution and molecular weight of the PMMA. In this study, the exact nanopatterns without bulges, and the advanced multi-tiered nanostructures were investigated. Furthermore, the neat multi-tiered nanometer scale molds through reworking process and the distinguishable replica structure with different four steps inside formed pattern were demonstrated. In conclusion, the AFM nano-indentation

process with bulge-free will be a key technology for future production of low-cost, complex, multi-tiered nanoscale devices.

5.2 Reference

[1] S.R. Cohen, A. Bitler, Use of AFM in bio-related systems, *Current Opinion in Colloid & Interface Science*, 13, **2008**, 316-325.

[2] T.G. Kuznetsova, M.N. Starodubtseva, N.I. Yegorenkov, S.A. Chizhik, R.I. Zhdanov, Atomic force microscopy probing of cell elasticity, *Micron*, 38, **2007**, 824-833.

[3] C. Shin, K. Kim, J. Kim, W. Ko, Y. Yang, S. Lee, C.S. Jun, Y.S. Kim, Fast, exact, and non-destructive diagnoses of contact failures in nano-scale semiconductor device using conductive AFM, *Scientific reports*, 3, **2013**, 2088.

[4] C. Shin, Nanoparticle alignment and nanoscale patterning study, **2010**.

[5] S.M. Salapaka, M.V. Salapaka, Scanning probe microscopy, *IEEE control systems*, 28, **2008**, 65-83.

[6] J. Park, C. Shin, M. Kim, J. Kim, J. Park, J. Kim, C. Jun, Y. Yim, J. Lee, Exact and reliable overlay metrology in nanoscale semiconductor devices using an image processing method, *J. Micro. Nanolithogr. MEMS MOEMS*, 13, **2014**, 041409-041409.

[7] J. Foucher, From CD to 3D sidewall roughness analysis with 3D CD-

AFM, in: Metrology, Inspection, and Process Control for Microlithography XIX, *International Society for Optics and Photonics*, **2005**, pp. 966-977.

국 문 초 록

스캐닝 프루브 현미경 (SPM)은 반도체 및 생체 분자 필름의 표면 구조 및 특성을 분석하는 데 널리 사용된다. SPM 방법의 장점은 시료 준비를 위한 어떠한 공정도 필요로 하지 않으며 조사 시료의 손상을 최소화한다는 것이다. 또한, 반도체 및 나노 바이오 디바이스와 관련된 산업의 성장은 나노 기술의 발전으로 이어지고 있다. 그래서 많은 연구자들은 반도체의 국소 도핑 프로파일, 반도체 박막의 표면 거칠기, 2 차원 재료의 일함수, 국소 표면 전하 분포, 유기-바이오 분자 박막, 나노 유체 장치의 표면 등을 분석하기위해 SPM 장비를 활용하고 있다.

최근에는 표면 분석 기능뿐만 아니라 여러가지 기능을 수행할 수 있는 원자력 현미경들이 등장하고 있다. 그 중에서도 저소음 원자력 현미경은 나노 스케일의 차세대 반도체 선폭을 측정하거나 초박막의 표면 검사에 이용될 수 있다. 따라서 산업적인 응용을 고려하여 한국표준과학연구원에서는 저소음 원자력 현미경을 개발하였고, 나노 인덴테이션 기능을 추가하여 R&D 수준에서 수십 나노의 정교한 패턴을 형성할 수 있는 공정 방법을 개발하고 있다.

저소음 원자력 현미경은 개발 배경의 특성상 내부적인 시료 이동 스테이지의 설치를 지양한다. 이는 저소음 원자력 현미경의 수취 신호 안정성

에 크게 기여하는 최선의 선택이긴 하지만, 검사 시료의 측정 영역을 축소시키는 약점으로 작용하고 있다. 따라서 이를 보완할 수 있는 독립적인 외부 스테이지는 필수적이라고 할 수 있기때문에, 이 논문에서는 중거리 이동 스테이지 개발을 통해 기준 시료의 임계 치수를 측정 할 수 있도록 개발하였다. 외부 4 축 스테이지의 최대 이동 길이는 10 mm이며, 특정 대상 영역의 이미지 스캐닝의 경우, 샘플을 외부 스테이지를 통해 마이크론 정확도의 위치 지정을 거친 후, PI XY piezo 스캐너를 이용하여 미세 위치 설정을 한다. 개발된 스테이지의 위치 에러는 재현성 실험을 통해 무시할 수 있음을 확인하였다. 이어서, 개선된 수직 평행 구조(IVPS)의 측벽을 측정하고 CD 측정의 반복성 및 재현성을 CDR30-EBD 팁을 사용하여 추정하였다. 마지막으로, 돌출 구조로 된 TGX1 샘플을 측정하여 팁 마모를 최소화 할 수 있음을 확인했다. 따라서 독립적인 외부 스테이지의 개발은 향후 넓은 영역을 스캔해야하는 여러가지 임무에 유용하게 적용될 수 있다.

산업의 in-line 시스템에서는 대면적 웨이퍼의 균일도를 검사하기 위해 광학적인 측정장비를 통해 박막 검사를 수행한다. 하지만 최근 차세대 반도체 산업에서는 고용량 및 저전력 디바이스의 출현으로 리소그래피 패턴이 점점 복잡해지고 절연체 박막의 두께는 수 나노 미터에서 서브 나노 미터 범위로 축소되고 있다. 따라서 가까운 미래의 in-line 공정에서는

반도체 장치의 생산 수율 향상을 위해서, 이들 박막의 두께뿐만 아니라 3 차원 (3D) 표면 정보를 검사하는 것이 필요해지고 있다. 실제 반도체 공정을 거친 표면의 거칠기는 향후 초박막 공정에 영향을 미치기도 하며, 표면이 거친 상태에서는 원자층 증착법(atomic layer deposition, ALD)에 의해 초박막 공정이 최적화되어 있다하더라도 소자에 영향을 줄 수 있기 때문이다. 따라서 박막의 성질을 정량화하고 국소적 표면 구조를 분석하기위해서는 원자력 현미경이 가장 적합한 분석법이라고 할 수 있다.

이 논문에서는 MOS 트렌지스터의 high-k 절연막인 하프늄 산화막 공정관리를 위한 방안으로 roughness scaling method를 고안하여 나노 스케일에서 최초로 임계거칠기(critical roughness, CR)을 정의하였다. 기판의 표면거칠기는 습식 식각 방식으로 진행하였으며, 하프늄 산화막을 얻기 위해 ALD 공정을 이용하였다. 이는 하부 층의 거칠기가 상부 층의 거칠기에 주는 영향성에 대한 연구이며, 이 정의를 통해 in-line 산화막 공정상에서 생산관리의 기준을 제시할 수 있게 되었다. 그리고 초박막 거칠기에 따른 MIM 다이오드 구조를 실현함으로써 이 연구에서 정의된 CR값이 실효성을 가짐을 확인하였다.

마지막으로 이 논문에서는 다기능성 원자현미경을 이용하여 나노 인덴테이션 리소그래피 연구를 진행하였다. 그 첫번째 연구는 전자빔 리소그래피로는 제작할 수 없는 바이오 필름 상에 나노 및 마이크로 패턴을 형

성함으로써 전자빔 리소그래피의 취약점을 보완할 수 공정 방법이 될 수 있음을 제시하는 것이며, 두번째 연구는 나노 인덴테이션의 근본적인 문제점인 벌지를 선택적으로 제거하는 연구이다.

우선 다기능성 원자현미경 활용의 첫번째 연구로는 바이오 필름상에 나노/마이크로 패턴을 형성하는 일이다. 이 패턴된 바이오 필름은 비행 시간 2 차 이온 질량 분석 (TOF-SIMS)의 화학적 성분 이미징 및 깊이 분석에 유용한 강력한 시료로 사용될 수 있다. TOF-SIMS 분석에서 Arn + 가스 클러스터 이온 소스 (GCIB)는 주로 표면 분석의 소스뿐만 아니라 낮은 손상 단면 및 분자 깊이 프로파일 링 실험을 위한 빠른 침식 속도를 갖는 침식 소스로서 널리 사용되었다. 그러나 SIMS 분석에서 3D depth profile에 대한 침식 메커니즘을 이해하려면 잘 정의 된 3D 유기 미세 패턴으로 보정해야 하는데, 이때 나노 인덴테이션 기술을 이용한다. 이 기법은 TOF-SIMS의 3D 화학적 성분 분석/이미징을위한 표준 바이오 시료로 사용될 것으로 기대한다.

두번째 인덴테이션 활용 연구는 탐침이 소프트 필름을 누를 때 발생하는 벌지를 선택적으로 제거하는 연구로써, PMMA 필름이 나노 패턴 형성층이 되도록 사용한다. 그동안 벌지는 인덴테이션 리소그래피의 발전을 저해하는 가장 큰 요인으로써 선택적인 제거가 어려운 것으로 알려져 있었다. 하지만 이 논문에서는 현상액을 이용한 간단한 방식으로 다단계의

벌지 없는 패터닝 방식을 최초로 소개함으로써 새로운 차원의 리소그래피 기법을 제안하고 있다. 또한 이 기법은 3차원 나노 패턴을 성공적으로 복제 몰드에 전사할 수 있으므로 공정 비용 절감 효과는 물론이고, 다양한 연구 분야에서 이를 활용할 수 있을 것으로 기대한다.

주요어: 원자력 현미경, 임계 거칠기, 원자층 증착법, 초박막, 벌지 제거 인덴테이션, 3D 리소그래피

학 번: 2010-31262